JETP Letters, Vol. 74, No. 9, 2001, pp. 445–448. From Pis'ma v Zhurnal Éksperimental'noĭ i Teoreticheskoĭ Fiziki, Vol. 74, No. 9, 2001, pp. 499–503.

BL Lacertae are Probable Sources of the Observed Ultrahigh Energy Cosmic Rays[1]

P. G. Tinyakov[1, 2] and I. I. Tkachev[2, 3]

[1] *Institute of Theoretical Physics, University of Lausanne, CH-1015 Lausanne, Switzerland*

[2] *Institute for Nuclear Research, Russian Academy of Sciences, pr. Shestidesyatiletiya Oktyabrya 7a, Moscow, 117312 Russia*

[3] *CERN Theory Division, CH-1211 Geneva 23, Switzerland*

Received 15 October, 2001

We calculate an angular correlation function between ultrahigh energy cosmic rays (UHECR), observed by Yakutsk and AGASA experiments, and the most powerful BL Lacertae objects. We find significant correlations with the probability of statistical fluctuation less than 10^{-4}, including penalty for selecting the subset of the brightest BL Lacs. We conclude that some of the BL Lacs are sources of the observed UHECR and present a list of the most probable candidates. © *2001 MAIK "Nauka/Interperiodica".*

PACS numbers: 98.70.Sa

Introduction. The identification of sources of ultrahigh energy cosmic rays (UHECR) is extremely important. Knowing the production sites of UHECR will be helpful in explaining the apparent absence of the Greisen–Zatsepin–Kuzmin (GZK) cutoff [1] by selecting a particular class of models. In the case of astrophysical origin, it will give invaluable information on physical conditions and mechanisms that may lead to the acceleration of particles to energies on the order of 10^{20} eV. In the case of extragalactic origin, it will provide direct information about the poorly known parameters that influence propagation of UHECR, such as extragalactic magnetic fields and universal radio background.

There are observational reasons to believe that UHECR are produced by compact sources. It has been known, for quite a while, that the observed highest energy cosmic rays contain doublets and triplets of events coming from close directions [2–4]. Our recent analysis [5] based on the calculation of the angular correlation function has shown that explanation of clusters by chance coincidence is highly improbable: the correlation function for Yakutsk events [6] with energies $E > 2.4 \times 10^{19}$ eV has an excess at 4° which would occur with a probability of 2×10^{-3} for the uniform distribution, while the correlation function for AGASA events [3, 7] with energies $E > 4.8 \times 10^{1}$ eV has an excess at 2.5° corresponding to a chance probability of 3×10^{-4}. The combined probability of the fluctuation in both sets is 4×10^{-6}. The autocorrelations as large as those should also imply a large correlation of these events with their actual sources. It is the purpose of this paper to identify these sources.

The clustering of UHECR by itself imposes certain constraints on the possible source candidates. With the observed fraction of events in clusters, the total number of sources can be estimated, along the lines of [8], to be on the order of several hundred. If the GZK cutoff is absent (or at energies below the cutoff), this estimate gives the number of sources in the entire Universe. Thus, to produce observed clustering, the extragalactic sources have to be extremely rare, as compared to ordinary galaxies. Taking 10^3 uniformly distributed sources for an estimate, the closest one is at the redshift $z \sim 0.1$.

Various astrophysical candidates such as neutron stars, supernovae, gamma-ray bursts, colliding galaxies, active galactic nuclei (AGN), lobes of radio galaxies, dead quasars, and others (for a review see [9] and references therein) have been proposed as sources of UHECR. A possible connection of highest energy cosmic rays with these objects was considered in [3, 4, 10]. In this paper, we study correlations of UHECR with BL Lacertae (BL Lac) objects, which comprise a subclass of AGN. Our motivations for selecting BL Lacs are as follows. If AGNs are sources, only those which have jets directed along the line of sight, or blazars, can correlate with observed UHECR events (regardless of the distance to a blazar in a world without GZK cutoff), since particles accelerated in a relativistic jet are strongly beamed. Blazars include BL Lacs and violently variable quasars with flat and highly polarized spectra. These spectral features give direct indication of a relativistically beamed jet very close to the line of sight. BL Lacs are a subclass of blazars characterized, in addition to the above spectral features which they share, by the (near) absence of emission lines in the spectra. This very important distinction indicates low density of ambient matter and radiation and, therefore,

[1] This article was submitted by the author in English.

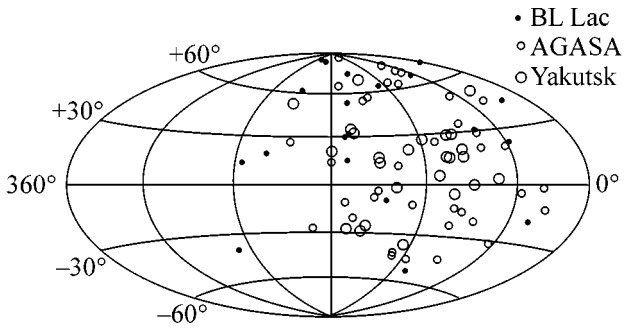

Fig. 1. The sky map (in Galactic coordinates) with 65 UHECR events (circles) and BL Lacertae objects with cuts (1).

more favorable conditions for the acceleration to the highest energies.

The most recent catalog of AGNs and quasars contains 306 confirmed BL Lacs [11]. While this is the richest catalog we are aware of, it still may be incomplete. However, this is not crucial for establishing correlations between BL Lacs and UHECR events. Correlations of BL Lacs with UHECR were not studied before. We show that these correlations do exist and are statistically significant.

Method and results. Our method is based on calculation of the angular correlation function and is similar to the one we used in [5]. For each BL Lac, we divide the sphere into concentric rings (bins) with a fixed angular size. We count the number of events falling into each bin and then sum over all BL Lacs, thus obtaining the numbers N_i (data counts). We repeat the same procedure for a large number (typically 10^6) of randomly generated sets of UHECR events. This gives the mean Monte-Carlo counts N_i^{MC}, the variance σ_i^{MC}, and the probability $p(\delta)$ to match or exceed the data count observed in the first bin. This probability is a function of the bin size δ. Peaks of $(N_i - N_i^{\mathrm{MC}})/\sigma_i$ or minima of $p(\delta)$ with respect to δ show angular scales on which the correlations are most significant.

The Monte-Carlo events are generated in the horizon reference frame with the geometrical acceptance

$$dn \propto \cos\theta_z \sin s\theta_z,$$

where θ_z is the zenith angle. Coordinates of the events are then transformed into the equatorial frame assuming random arrival time. This transformation depends on the latitude of the experiment, so that events simulating different experiments are generated separately. The distribution of the generated Monte-Carlo events in declination and right ascension reproduces well the distribution of experimental data.

We have shown in [5] that autocorrelations are most significant for the two sets of UHECR events: 26 Yakutsk events with energy $E > 2.4 \times 10^{19}$ eV and 39 AGASA events with energy $E > 4.8 \times 10^{19}$ eV. If BL Lacs are sources of UHECR, their correlations with UHECR should be particularly large for these two sets. Assuming that energies of the events are not important for correlations at small angles, we combine them together in one set of 65 events.

Since acceleration of particles to energies of order 10^{20} eV typically requires extreme values of parameters, probably, not all BL Lacs emit UHECR of the required energy. We assume that this ability is correlated with optical and radio emissions and select the most powerful BL Lacs by imposing cuts on redshift, apparent magnitude, and 6-cm radio flux. For more than a half of BL Lacs, the redshift is not known. It is generally expected that these BL Lacs are at $z > 0.2$. We include them in the set. The cuts

$$\begin{gathered} z > 0.1 \text{ or unknown; mag } < 18; \\ \text{energy flux at 6-cm wavelenght } F_6 > 0.17 \text{ Jy} \end{gathered} \qquad (1)$$

leave 22 BL Lacs, which are shown in Fig. 1 together with 65 cosmic rays from the combined set. The dependence on cuts is discussed below.

As one can see from Fig. 1, 2 of the 22 BL Lacs coincide with the 2 triplets of UHECR events, 1 coinciding with a doublet and 2 BL Lacs lying close to single events. This is reflected in the correlation function, which is plotted in Fig. 2 for the bin size 2.5°. It has 8 events in the first bin, while 1.25 is expected for the uniform distribution. The probability of such an excess is 2×10^{-5}. BL Lacs and UHECR events contributing to this correlation are listed in the table. Note that at large angles the correlation function fluctuates around zero, which shows that the acceptance in the Monte-Carlo simulation is chosen correctly.

The probability $p(\delta)$ as a function of angular separation δ is shown in Fig. 3. It has a minimum at 2.5°. For comparison, the smooth curve shows the behavior expected in the case if 9 events out of 65 come from BL Lacs (assuming that accuracy of angle determination is 1.8° and distribution of errors is Gaussian).

The small angular size of the peak in the correlation function, compatible with the experimental angular resolution, suggests that UHECR events responsible for these correlations are produced by neutral primary particles. Indeed, if the primaries were charged, they

Names and coordinates (Galactic longitude, latitude, and redshift) of BL Lacs plotted in Fig. 1, which fall within 3° from some UHECR event (their energies are listed in the last column)

Name	l	b	z	$E/10^{19}$ eV
1ES 0806 + 524	166.25	32.91	0.138	3.4; 2.8; 2.5
RX J10586 + 5628	149.59	54.42	0.144	7.76; 5.35
2EG J0432 + 2910	170.52	–12.6	–	5.47; 4.89
OT 465	74.22	31.4	–	4.88
TEX 1428 + 370	63.95	66.92	0.564	4.97

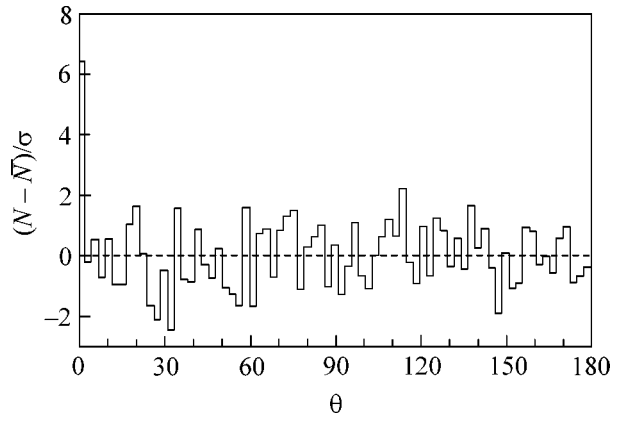

Fig. 2. The angular correlation function between the combined set of UHECR and BL Lac set (1).

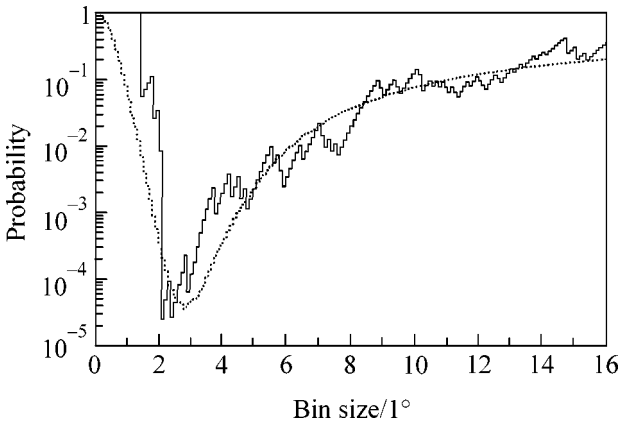

Fig. 3. The dependence of the probability $p(\delta)$ on the bin size δ for the combined set of UHECR and BL Lac set (1).

would have been deflected in the Galactic magnetic field by 3°–7°, depending on the arrival direction, particle energy, and the model of magnetic field, so that correlations at 2.5° would be destroyed.

Discussion. We have seen that 22 bright BL Lacs and 65 cosmic rays from the combined set are strongly correlated; the probability of finding 8 or more out of 65 randomly generated cosmic rays within 2.5° of any of the BL Lacs is 2×10^{-5}. Should one conclude that BL Lacs are sources of UHECR? Or is it possible that the above correlation may be an artifact of our selection procedure? Let us discuss possible loopholes.

The first potential problem source is the incompleteness of the BL Lac catalog and nonuniform coverage of the sky. Indeed, 22 BL Lacs selected by cuts (1) almost all lie in the Northen hemisphere due to observational bias. However, it is easy to understand that, unlike many other astrophysical problems, the incompleteness of the BL Lac catalog is not essential for establishing the *fact of correlations* with UHECR. The method we use is suited for any set of potential sources, regardless of their distribution over the sky (including extreme cases such as only one source, or a compact group of several sources). This is guaranteed by using the same set of sources with real data and with each Monte-Carlo configuration.

The second potential problem is related to the fact that there exist strong autocorrelations in the UHECR set, while Monte-Carlo events are not correlated. One may wonder if the observed correlation with BL Lacs is (partially) due to autocorrelations of UHECR. To see whether this effect is negligible in our case, we performed test Monte-Carlo simulations with configurations containing the same number of doublets and triplets as the real data and being random in other respects. We found practically no difference between the two methods.

Finally, there is the issue of cuts and the related issue of the selection of catalogs. It is cause for concern that, by adjusting several cuts and searching in several catalogs, a probability as small as $p_{\min} \sim 10^{-5}$ can be found with any set of astrophysical objects, even with those which have nothing to do with UHECR. So, the question is how easily can the low values of $p_{\min}$, be obtained within the adopted procedure of cuts? This question can be studied quantitatively by assigning a proper penalty to each try in such a way that the resulting probability gives a true measure for the correlations in question to be a statistical fluctuation. For the case at hand, we have found that, when proper penalties are assigned, the resulting probability is larger than $p_{\min}$ by about an order of magnitude. In other words, one would have to try thousands of catalogs to find a correlation as significant as the one we have found for BL Lacs. The procedure of penalty calculation and the resulting significance of correlations are presented below.

In fact, we did not search for correlations with other catalogs of astrophysical objects. Thus, no penalty is associated with that. Similarly, we did not adjust the set of cosmic rays (as explained before, it was selected in [5] on the basis of the most significant autocorrelations). But we do adjust cuts in the BL Lac catalog. Therefore, we should assign a penalty factor to this adjustment.

It is clear that some cuts have to be made because 65 events may have at most 65 sources among 306 BL Lacs in the catalog (probably, much less). In our calculations, we imposed cuts on redshift, magnitude, and 6-cm radio flux. The cut on redshift is motivated by the expected total number of sources; we did not adjust this cut to minimize the probability. Cuts on magnitude and radio flux were adjusted. The corresponding penalty can be calculated in the following way (cf. [5]). A random set of cosmic rays should be generated and treated as real data; i.e., minimum probability $p_{\min}$ is searched for by adjusting the cuts in the BL Lac catalog in exactly the same way as it was done for the real data. This should be repeated many times, giving different $p_{\min}$ each time. The number of occurrences of a given value of $p_{\min}$ is then calculated as a function of $p_{\min}$. This gives the probability (we call it p_{cor}) that the

adjustment of the cuts in BL Lac catalog produces $p \le p_{min}$ with a random set of cosmic rays. The probability p_{cor} is a correct measure of the significance of correlations. We define $p_{cor}/p_{min} > 1$ as the penalty factor.

We calculated p_{cor} with 10^5 random sets of cosmic rays. We have found that the penalty grows at small p_{min} and approaches a constant value in the limit $p_{min} \longrightarrow 0$ (for this reason, it is more convenient to define the penalty factor than to work in terms of p_{cor}). For the real set of UHECR, $p_{min} = 4 \times 10^{-6}$ and is reached with the cuts

$$z > 0.1 \text{ or unknown}; \quad \text{mag} < 16; \quad F_6 > 0.17 \text{ Jy}. \quad (2)$$

They leave 5 BL Lacs, 2 of which coincide with triplets. (In the previous section, different cuts are presented, because, with similar significance, they include more potential sources.) This probability should be multiplied by the penalty factor. We found that the penalty factor is $\simeq 15$ at $p_{min} \simeq 10^{-6}$.[2] This gives $p_{cor} = 6 \times 10^{-5}$, which is the probability that the correlation we have found is a statistical fluctuation.

Conclusions. The significant correlations between UHECR and BL Lacs imply that at least some of the BL Lacs are sources of UHECR. The most probable candidates can be seen in Fig. 1 and are listed in the table. Two BL Lacs, 1ES 0806+524 and RX J10586+5628, coincide with triplets of UHECR events (in the second case, the third event of a triplet is at 4.5° and is not listed in the table). Both of them are at a distance of ~600 Mpc from the Earth. The next probable candidate 2EG J0432+2910 has unknown redshift.

The correlations at small angles are difficult to explain by charged primary particles. Within the Standard Model, the only two neutral candidates are photon and neutrino. Photon attenuation length at $E < 10^{20}$ eV is much smaller (see, e.g., [9]) than the distance to even the closest BL Lac. However, photons cannot be ruled out yet if one assumes the presence of sources at $d \sim$ 600 Mpc and the "extreme" astrophysical conditions: primary particles accelerated to $E > 10^{23}$ eV with "hard" spectrum $\sim E^{-\alpha}$ and $\alpha < 2$ and extragalactic magnetic fields $B < 10^{-11}$ G [12]. Neutrino models [13] require similar assumptions, except that constraints on the magnetic field are relaxed for "pure" neutrino sources and there is no constraint on the distance to the sources. However, if pure neutrino sources cannot be arranged, the model effectively becomes "photonic" [12]. If astrophysical difficulties can be overcome, these models will be appealing candidates for the solution of the UHECR puzzle. Alternatively, one may resort to a new physics, e.g., violation of the Lorentz invariance [14].

Independent cross-checks are necessary to determine whether particular objects are sources of UHECR. One of these cross-checks could be a coincidence of the arrival time of events contributing to small angle correlations with periods of activity of candidate BL Lacs. Dedicated monitoring of these BL Lac may be suggested. It is also important to analyze possible specific properties of air showers initiated by these events.

We are grateful to S.L. Dubovsky, K.A. Postnov, M.E. Shaposhnikov, and D.V. Semikoz for valuable comments and discussions. This work was supported by the Swiss Science Foundation (grant no. 21-58947.99) and the INTAS (grant no. 99-1065).

[2] This number does not include penalty for the adjustment of the bin size, because minimum of $p(\delta)$ is consistent with the angular resolution. Corresponding factor is ≈ 4.

REFERENCES

1. K. Greisen, Phys. Rev. Lett. **16**, 748 (1966); G. T. Zatsepin and V. A. Kuzmin, Pis'ma Zh. Éksp. Teor. Fiz. **4**, 144 (1966) [JETP Lett. **4**, 99 (1966)].
2. X. Chi *et al.*, J. Phys. G **18**, 539 (1992); N. N. Efimov and A. A. Mikhailov, Astropart. Phys. **2**, 329 (1994).
3. M. Takeda *et al.*, astro-ph/9902239.
4. Y. Uchihori *et al.*, Astropart. Phys. **13**, 151 (2000); astro-ph/9908193.
5. P. G. Tinyakov and I. I. Tkachev, Pis'ma Zh. Éksp. Teor. Fiz. **74**, 3 (2001) [JETP Lett. **74**, 1 (2001)]; astro-ph/0102101.
6. *Catalogue of Highest Energy Cosmic Rays*, Ed. by A. Inoue and E. Sakamoto (World Data Center C2 for Cosmic Rays, Institute of Physical and Chemical Research, Wako, Saitama, 1988), No. 3.
7. N. Hayashida *et al.*, Astrophys. J. **522**, 225 (1999); astro-ph/0008102.
8. S. L. Dubovsky, P. G. Tinyakov, and I. I. Tkachev, Phys. Rev. Lett. **85**, 1154 (2000); astro-ph/0001317.
9. P. Bhattacharjee and G. Sigl, Phys. Rep. **327**, 109 (2000).
10. J. Elbert and P. Sommers, Astrophys. J. **441**, 151 (1995); G. Farrar and P. Biermann, Phys. Rev. Lett. **81**, 3579 (1998); A. Virmani, S. Bhattacharya, P. Jain, *et al.*, astro-ph/0010235; G. Sigl, D. F. Torres, L. A. Anchordoqui, and G. E. Romero, Phys. Rev. D **63**, 081302 (2001); astro-ph/0008363; S. S. Al-Dargazelli *et al.*, J. Phys. G **22**, 1825 (1996); G. R. Farrar and T. Piran, astro-ph/0010370; A. A. Mikhailov, in *Proceedings of the 26th International Cosmic Ray Conference, Salt Lake City, 1999*, Vol. 3, p. 268; A. A. Mikhailov and E. S. Nikiforova, Pis'ma Zh. Éksp. Teor. Fiz. **72**, 229 (2000) [JETP Lett. **72**, 157 (2000)].
11. M. P. Veron-Cetty and P. Veron, *Quasars and Active Galactic Nuclei*, ESO Scientific Report 9th ed. (2000).
12. O. E. Kalashev, V. A. Kuzmin, D. V. Semikoz, and I. I. Tkachev, astro-ph/0107130.
13. T. J. Weiler, Phys. Rev. Lett. **49**, 234 (1982); D. Fargion, B. Mele, and A. Salis, Astrophys. J. **517**, 725 (1999); S. Yoshida, G. Sigl, and S. Lee, Phys. Rev. Lett. **81**, 5505 (1998); J. J. Blanco-Pillado, R. A. Vazquez, and E. Zas, Phys. Rev. D **61**, 123003 (2000); G. Gelmini and A. Kusenko, Phys. Rev. Lett. **82**, 5202 (1999); hep-ph/9902354.
14. S. R. Coleman and S. L. Glashow, Phys. Rev. D **59**, 116008 (1999); hep-ph/9812418; S. L. Dubovsky and P. G. Tinyakov, astro-ph/0106472.

JETP Letters, Vol. 74, No. 9, 2001, pp. 449–452. Translated from Pis'ma v Zhurnal Éksperimental'noĭ i Teoreticheskoĭ Fiziki, Vol. 74, No. 9, 2001, pp. 504–507.

A Search for the Effects of Nuclear Matter in Backward Pion–Deuteron Quasielastic Scattering by ^{6}Li

B. M. Abramov, Yu. A. Borodin, S. A. Bulychjov, I. A. Dukhovskoĭ, A. P. Krutenkova, V. V. Kulikov, M. A. Matsyuk, I. A. Radkevich, E. N. Turdakina*, and A. I. Khanov

Institute of Theoretical and Experimental Physics, ul. Bol'shaya Cheremushkinskaya 25, Moscow, 117259 Russia

**e-mail: turdakina@vxitep.itep.ru*

Received September 27, 2001

Results of a kinematically complete experiment on backward $\pi^- d$ quasielastic scattering by ^{6}Li are presented. The experiment was carried out at the ITEP 3-m magnetic spectrometer with pion beams of momenta 0.72, 0.88, and 1.28 GeV/c. The Fermi-motion parameters of a quasideuteron cluster and the effective number of quasideuterons in ^{6}Li are determined for the $^6\mathrm{Li}(\pi^-, \pi^- d)^4\mathrm{He}$ reaction. These values agree well with the proton- and electron-beam measurements. The possibility of observation of the effects of deuteron wave-function modification in nuclear matter is discussed for this reaction. © *2001 MAIK "Nauka/Interperiodica".*

PACS numbers: 25.70.Bc; 25.80.Hp

The mechanism of pion–deuteron elastic scattering with high momentum transfer is one of the as yet unsolved problems of relativistic nuclear physics. One such attempt at describing experimental data for $-t = 3$–7 $(\mathrm{GeV}/c)^2$ (c is the speed of light) consists in the inclusion of the 6-quark component of deuteron wave function (see [1] and references therein). Although other approaches to the πd-scattering problem are known [2], the introduction of a 6-quark component seems to be quite attractive, because it provides a unified approach to the description of other deuteron reactions with high momentum transfer. Chiral soliton models also point to the important role of the dibaryon (or 6-quark) configurations [3]. According to Battye and Sutcliffe's calculations [4], the lowest-energy configurations of chiral fields with small baryon numbers, including $B = 6$, can be formed from several deformed configurations with $B = 2$. With this approach, it is natural to assume that the admixture of a 6-quark component is a function (possibly, rapidly increasing) of the deuteron nuclear density. The deuteron density may change in nuclei with a deuteron-cluster structure. In this respect, the ^{6}Li nucleus with the pronounced d–α cluster structure is most appropriate. Therefore, a comparison of the cross sections for πd elastic scattering by free deuteron and πd quasielastic scattering by deuteron cluster (quasideuteron) in ^{6}Li with large momentum transfer can provide new information about both backward πd scattering and the modification of the deuteron wave function in nuclear matter. Single-energy measurements can hardly be interpreted unambiguously because absorption effects introduce considerable uncertainties. As for the comparison of energy dependences of elastic and quasielastic scattering over a wide energy range, it is, to a great extent, free from these uncertainties. We undertook the first step in this direction, because kinematically complete experiments on quasielastic deuteron knock-out from nuclei by pions have not been performed to date (only one experiment on measuring inclusive spectra [5] and several proton- and electron-beam experiments with smaller momentum transfers are available [6–8]). We were the first to measured the quasielastic deuteron knock-out by pions in the reaction

$$\pi^- + {}^6\mathrm{Li} \longrightarrow d + \pi^- + \mathrm{X} \qquad (1)$$

in the angular range from 145° to 180° in the c.m.s. of pion–deuteron elastic scattering for three beam momenta, 0.72, 0.88, and 1.28 GeV/c [the maximal momentum transfers to deuteron were 1.2, 1.8, and 2.6 $(\mathrm{GeV}/c)^2$, respectively].

The experiment was carried out using a 3-m magnetic spectrometer (see, e.g., [1]) with a pion beam from the ITEP 10-GeV proton synchrotron. Nuclear targets were placed near the center of a $3 \times 1 \times 0.5$-m dipole magnet. One half of the magnet was used as a spectrometer for the forward-emitted deuterons. The other half was used as a spectrometer for the backward-scattered and beam pions. A ^{6}Li-enriched target (90.4% ^{6}Li and 9.6% ^{7}Li) was placed in a thin-walled $\varnothing 8 \times 9.5$-cm container. The time-of-flight identification of deuterons was carried out using a hodoscope system of scintillation counters with an area of 1.5 m^2 placed at 6 m from the target. All three above-mentioned particles (deuteron and pions) were detected in spark chambers, and their vector momenta were determined from the geometrically reconstructing tracks in a magnetic field of the spectrometer. An important point was that the

0021-3640/01/7409-0449$21.00

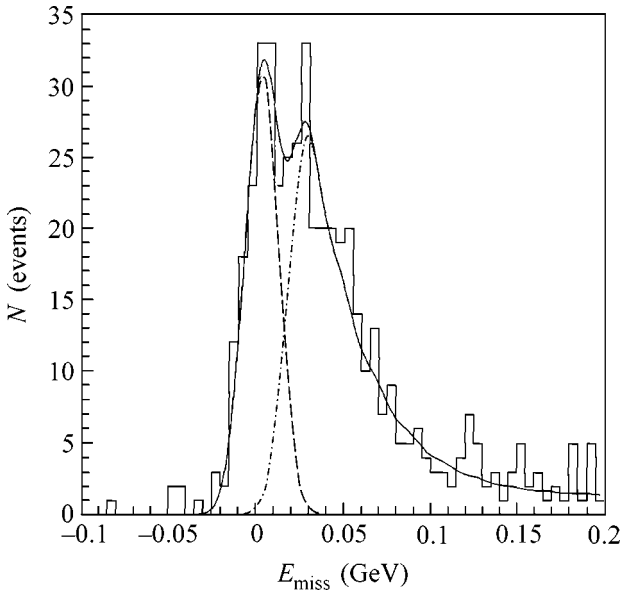

Fig. 1. Distribution of the events of reaction (1) in E_{miss} for $p_0 = 0.72$ GeV/c. The solid line is the approximation by the sum of two processes. The dashed line is for a peak at $E_{miss} = 1.5$ MeV corresponding to reaction (4). Fitting is carried out using a Gaussian function with a resolution of 9.5 MeV. The dash–dotted line is a continuous spectrum of exponentially decreasing shape at $E_{miss} > 22$ MeV corresponding to the ^{4}He disintegration. Fitting is performed with allowance for experimental resolution.

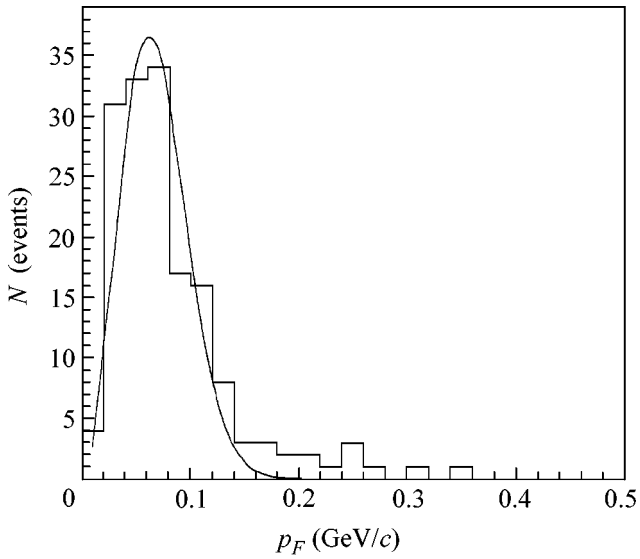

Fig. 2. Fermi-momentum ($\mathbf{p}_F$) distribution of a quasideuteron in ^{6}Li in reaction (4) for $p_0 = 0.72$ GeV/c ($-0.020 \le E_{miss} \le 0.015$ GeV). The solid line is the approximation of the spectrum by the Gaussian function $\exp(-p_F^2/\kappa^2)p_F^2$ with allowance for the instrumental efficiency. The fitting parameter was found to be $\kappa = 64 \pm 4$ MeV/c.

experiment simultaneously provided data on pion–deuteron elastic scattering by free deuterons in the difference experiment with heavy-water (D_2O) and water (H_2O) targets. The data obtained for the elastic pion–deuteron scattering cross section agreed well with the available data [1, 9, 10]. Measurements with the heavy-water target were used to check the simulation of the experiment for correctness and to determine the experimental Fermi-momentum resolution for quasideuterons (17 MeV/c) and the excitation-energy resolution (9.5 MeV) for the residual nucleus.

For the events of reaction (1), we calculated the Fermi momentum of the deuteron cluster

$$\mathbf{p}_F = \mathbf{p}_0 - \mathbf{p}_d - \mathbf{p}_\pi \quad (2)$$

and the missing energy (or the excitation energy of the residual nucleus X)

$$E_{miss} = T_0 - T_\pi - T_d - T_X. \quad (3)$$

Here, T is the kinetic energy; the subscripts 0, π, d, and X denote the initial and final pions, the deuteron, and the residual nucleus, respectively; and $T_X = (\mathbf{p}_F)^2/2M$, where M is the mass of ^{4}He nucleus.

Figure 1 shows the missing-energy (E_{miss}) distribution of the detected events of reaction (1) for 0.72 GeV/c. The shape of this spectrum is well known [8]. It consists of a line at $E_{miss} = 1.5$ MeV corresponding to the knock-out of the deuteron cluster

$$\pi^- + {}^6\mathrm{Li} \longrightarrow d + \pi^- + {}^4\mathrm{He}, \quad (4)$$

and a continuous spectrum at $E_{miss} \ge 22$ MeV corresponding to the deuteron knock-out from an α cluster and the disintegration of the residual nucleus. With allowance made for experimental resolution, this shape, with an exponentially decreasing continuous spectrum, closely reproduces our data.

Figure 2 shows the Fermi-momentum distribution of events at -0.020 GeV $\le E_{miss} \le 0.015$ GeV for 0.72 GeV/c. The plane-wave impulse approximation (PWIA) and the Monte Carlo method were used to approximate it by a Gaussian distribution $\exp(-p_F^2/\kappa^2)p_F^2$ in the spherical coordinate system. The fitted Gaussian distribution parameter was found to be $\kappa = 64 \pm 4$ MeV. Using this parametrization of Fermi-momentum distribution, we calculated the expected number of events for reaction (4) in the PWIA and, after comparing with the observed number of events, determined the product $n_d(d\sigma/d\Omega)$, where n_d is the effective number of ^{6}Li deuterons involved in reaction (4) and $d\sigma/d\Omega$ is the c.m.s. differential cross section for backward pion–deuteron elastic scattering by a quasideuteron in ^{6}Li. The n_d values calculated with

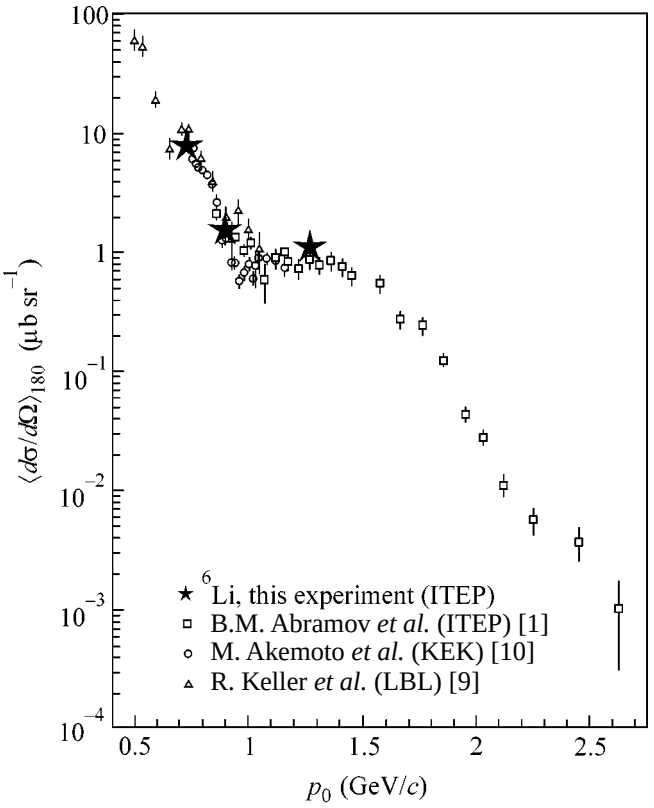

Fig. 3. Energy dependence of the cross section for backward pion–deuteron elastic scattering. The black stars are our data obtained from the product $n_d(d\sigma/d\Omega)$ (see text).

$d\sigma/d\Omega$ taken equal to the known free-deuteron cross sections are given in the table. The data of other proton- and electron-beam experiments are also presented in the table. All data on n_d agree well with each other and with the theoretical calculations [6–8] for n_d with inclusion of the absorption effects in the initial and final states. Unfortunately, such calculations are lacking for the conditions of our experiment. The energy dependence of n_d was measured only in our experiment; according to our measurements, n_d is constant within experimental error. Therefore, in the energy and momentum-transfer ranges studied, we do not observe nuclear-matter effects on the pion–deuteron elastic scattering cross section. This is illustrated in Fig. 3, where our data on the product $n_d(d\sigma/d\Omega)$ are presented together with the energy dependence of backward pion–deuteron elastic scattering by a free deuteron [1, 9, 10]. It is seen that the cross sections for pion–deuteron elastic and quasielastic scattering agree well with each other. The parameters κ of quasideuteron Fermi motion in ^{6}Li (see table) are in poorer agreement with each other than are the n_d values. This is possibly due to the distortion effects, which were taken into account in none of the experiments, except for [8]. It is quite possible that a considerably more complicated analysis of the data in the distorted-wave impulse approximation would reduce these discrepancies between the experiments.

Table

T_0, GeV	Beam	κ, MeV/c	n_d (PWIA)	Reference
0.59	p	73 ± 1.6	0.78 ± 0.10	[7]
0.67	p	51.5 ± 2.5	0.83 ± 0.08	[6]
0.48	e	45*	0.73 ± 0.07	[8]
0.59	π	64 ± 4	0.74 ± 0.07	**
0.75	π		0.77 ± 0.15	**
1.15	π		1.26 ± 0.44	**

* In this work, the shapes of Fermi-momentum distribution were more complex; for this reason, we present our estimate of the Gaussian distribution parameter.

** This experiment.

Let us summarize the conclusions of the experiment.

(i) The quasielastic deuteron knock-out from nuclei was studied in a kinematically complete experiment with a pion beam.

(ii) The Fermi-motion parameters determined for a quasideuteron cluster in the ^{6}Li nucleus are in reasonable agreement with the data obtained with proton and electron beams.

(iii) The energy dependence of quasielastic deuteron knock-out from ^{6}Li in the beam-momentum range from 0.72 to 1.28 GeV/c and momentum-transfer range $-t$ = 1.2–2.6 (GeV/c)^2 coincides, within experimental error, with the energy dependence of backward pion–deuteron elastic scattering.

(iv) The smallness of the cross section did not allow us to extend our measurements to the range $-t > 3$ (GeV/c)^2, which is the most interesting for studying the effects of deuteron wave-function modification in nuclear matter.

We are grateful to the staffs of the 3-m spectrometer, the ITEP accelerator, and the PSP-2 group for assistance in conducting the experiment, as well as to L.A. Kondratyuk for stimulating discussions. This work was supported in part by the Russian Foundation for Basic Research, project nos. 00-02-17163 and 00-15-96545.

REFERENCES

1. B. M. Abramov, S. A. Bulychjov, B. L. Druzhinin, *et al.*, Nucl. Phys. A **542**, 579 (1992); Phys. Lett. B **189**, 295 (1987).

2. H. Garcilazo and L. Mathelitsh, Phys. Rev. C **60**, 027001 (1999).
3. V. B. Kopeliovich, Yad. Fiz. **58**, 1317 (1995) [Phys. At. Nucl. **58**, 1237 (1995)]; Zh. Éksp. Teor. Fiz. **120**, 499 (2001) [JETP **93**, 435 (2001)].
4. R. A. Battye and P. M. Sutchiffe, Phys. Rev. Lett. **79**, 363 (1997).
5. B. M. Abramov, É. A. Aĭrapetov, L. S. Bagdasaryan, *et al.*, Yad. Fiz. **38**, 823 (1983) [Sov. J. Nucl. Phys. **38**, 491 (1983)].
6. D. Albrecht, M. Csatlos, J. Ero, *et al.*, Nucl. Phys. A **338**, 477 (1980).
7. P. Kitching, W. C. Olsen, H. S. Sherif, *et al.*, Phys. Rev. C **11**, 420 (1975).
8. R. Ent, H. P. Block, J. F. A. van Hienen, *et al.*, Phys. Rev. Lett. **57**, 2367 (1986).
9. R. Keller, D. G. Grabb, J. R. O'Fallon, *et al.*, Phys. Rev. D **11**, 2389 (1975).
10. M. Akemoto, K. Baba, I. Endo, *et al.*, Phys. Rev. Lett. **50**, 400 (1983).

Translated by R. Tyapaev

JETP Letters, Vol. 74, No. 9, 2001, pp. 453–455. From Pis'ma v Zhurnal Éksperimental'noĭ i Teoreticheskoĭ Fiziki, Vol. 74, No. 9, 2001, pp. 508–510.

Anatomy of Isolated Monopole in Abelian Projection of *SU*(2) Lattice Gauge Theory[1]

V. A. Belavin, M. I. Polikarpov, and A. I. Veselov

Institute of Theoretical and Experimental Physics, ul. Bol'shaya Cheremushkinskaya 25, Moscow 117259, Russia

Received October 4, 200l

We study the structure of isolated static monopoles in the maximal Abelian projection of SU(2) lattice gluodynamics. Our estimation of the monopole radius is: $R^{\text{mon}} \approx 0.06$ fm. © *2001 MAIK "Nauka/Interperiodica".*

PACS numbers: 11.15.-q; 12.38.-t

1. The monopole confinement mechanism in *SU*(2) lattice gauge theory is confirmed by many numerical calculations (see, e.g., reviews [1]). In the maximal Abelian projection, monopole currents form one big cluster and several small clusters. The big cluster—infrared (IR) cluster—percolates and has a nontrivial fractal dimension, $D_f > 1$ [2]. The properties of small—ultraviolet (UV)—clusters differ much from those of the IR cluster; it can be shown that the IR monopole cluster is responsible for the confinement of quarks [3]. As was shown in a recent publication [4], the structures of IR and UV monopoles are completely different, and monopoles in IR clusters are condensed due to their special anatomy. In this publication, we study the structure of Abelian monopoles in *SU*(2) lattice gauge theory in a different way than was done in [4]. We study the structure of isolated monopoles; the results show that the nontrivial monopole anatomy plays a crucial role in the confinement phenomenon.

2. The plaquette action of compact electrodynamics (cQED),

$$S^P_{cQED} = \beta_{U(1)} \cos\theta_P, \tag{1}$$

is close to the action of *SU*(2) lattice gauge theory in the maximal Abelian projection at small values of bare charge *g* (in the continuum limit of gluodynamics). The proof is as follows. By definition, the maximal Abelian projection corresponds to the maximization of the functional *R* with respect to all gauge transformations Ω:

$$\max_{\Omega} R[U^{\Omega}_l], \quad U^{\Omega}_l = \Omega^+ U_l \Omega,$$
$$R[U_l] = \sum_l \mathrm{Tr}[\sigma_3 U^+_l \sigma_3 U_l] = \sum_l \cos 2\varphi_l. \tag{2}$$

Here we use the standard parametrization for the link matrix, $U_{l,11} = U^*_{l,22} = \cos\varphi_l e^{i\theta_l}$, $U_{l,12} = U^*_{l,21} = \sin\varphi_l e^{-i\chi_l}$. Thus, the maximization of *R* in Eq. (2) corresponds to the maximization of the moduli of the diagonal elements $U_{l,11}$, $U_{l,12}$. The *SU*(2) plaquette action is $S^P_{SU(2)} = \beta \times \frac{1}{2}\mathrm{Tr}\,U_p = \beta\cos\theta_l$, and, at large values of β, in the maximal Abelian projection $\cos\varphi_l$ is close to unity [due to Eq. (2)], φ_l is small, and *SU*(2) plaquette action has the form

$$S^P_{SU(2)} = \beta[\cos\theta_P \cos\varphi_1 \cos\varphi_2 \cos\varphi_3 \cos\varphi_4 + O(\sin\varphi_l)]. \tag{3}$$

3. The larger the value of β the smaller is $\sin\varphi_l$, and $S^P_{SU(2)}$ (3) coincides with S^P_{cQED} (1) in the limit $\beta \longrightarrow \infty$. On the one hand, at small values of the bare charge [at large values of $\beta_{U(1)}$] the compact electrodynamics is in the deconfinement phase and the gluodynamics is in the confinement phase; on the other hand, the actions of both theories are close to each other. The explanation of this paradox was given in [5, 4], where it was shown that the action of the off-diagonal gluons S^{off} on the plaquettes near the monopole from IR clusters is negative and the full non-Abelian action $S^{SU(2)} = S^{\text{off}} + S^{\text{Abel}}$ is smaller than the Abelian part of the action. The standard qualitative proof of the existence of the deconfinement phase transition in cQED is the representation of the partition function as the sum over the monopole trajectories of length *L*:

$$\mathcal{Z} = \sum_L \exp\{-\beta L c\}(7)^L. \tag{4}$$

Here, *c* is the action of the unit length of monopole trajectory and 7^L is the entropy of the line of length *L* drawn on 4*D* hypercubic lattice. It is clear that at β =

[1] This article was submitted by the authors in English.

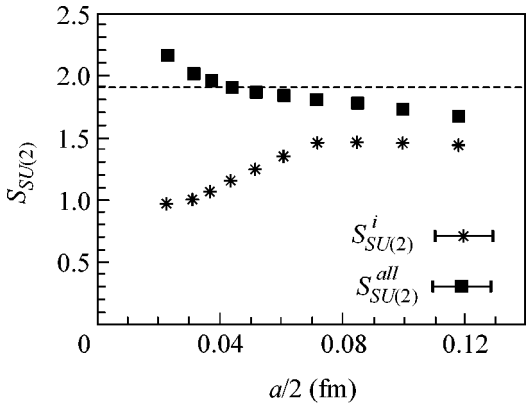

The dependence of (stars) $S^i_{SU(2)}$ and (squares) $S^{all}_{SU(2)}$ on $a/2$. The dashed line corresponds to $S = \ln 7$.

$\beta_c \equiv \ln 7/c$ the phase transition exists in the sum (4). This phase transition is absent in lattice gluodynamics, since in this case the monopoles have nontrivial structure and the action of the unit of monopole trajectory in lattice units depends on β: $c = c(\beta)$; the sum (4) is always divergent; and the monopoles are condensed and form the percolating cluster. The monopole condensation was proven in gluodynamics by several independent calculations [6].

4. In [4], the average nonabelian action on the plaquettes near the monopole trajectory in IR clusters was measured. Since the lattice spacing a depends on β, the calculations at various β correspond to the measurement of field strength at various distances, $a(\beta)/2$ from the monopole center. Below, we present the results of different measurements; we calculate the average field strength on the plaquettes closest to the monopole center for the monopoles satisfying the following two conditions:

(i) the link with the monopole current has the same direction as the previous and subsequent monopole current links;

(ii) there are no other monopoles at a distance less than $2a$ from the considered monopole, except for the monopoles discussed in item (i).

Thus, we study "static" and "standing-alone" monopoles; we call such monopoles *isolated* monopoles. The results of calculations are shown in the figure, where we plot the dependence of $S^i_{SU(2)} = 6\beta \times \frac{1}{2}(\langle \mathrm{Tr} U_P^{\mathrm{imon}} \rangle - \langle \mathrm{Tr} U_P \rangle)$ on $a/2$; U_P^{imon} are the plaquette matrices corresponding to the plaquettes closest to the isolated monopole, the normalization of $S^i_{SU(2)}$ is such that it exactly corresponds to the action of the unit length of monopole trajectory. If $S^i_{SU(2)} < \ln 7$, the isolated monopoles are condensed [see discussion of the partition function (4)]. In the figure, we also show the quantity $S^{all}_{SU(2)} = 6\beta \times \frac{1}{2}(\langle \mathrm{Tr} U_P^{\mathrm{allmon}} \rangle - \langle \mathrm{Tr} U_P \rangle)$, where U_P^{allmon} is the matrix corresponding to the plaquettes closest to all monopoles (isolated and not isolated).

The main conclusion from the figure is that the action of isolated monopoles decreases when the monopole center is approached and that these monopoles are condensed. Our numerical results also show that the *Abelian* part of the action of isolated monopoles increases when the monopole center is approached. Thus, the contribution of the off-diagonal gluons to the non-Abelian action of monopole is negative, and, for this reason, these monopoles differ from the monopoles in cQED and are condensed at any value of β.

5. Following [4], we can estimate the radius R_m of an isolated monopole as a point where the derivative of function $S^i_{SU(2)}(a/2)$ is maximal. We thus get $R_m \approx 0.065$ fm. Note that other dimensional numbers characterizing the gluodynamic vacuum are an order of magnitude larger. For example, the average intermonopole distance [4], which can be estimated from the results of [3], is $R_m \approx 0.5$ fm; the width of the Abelian confining flux tube is $R_t \approx 0.3$ fm [7]; and the average instanton radius is $R_I \approx 0.3$ fm (see [8] and references therein). Thus, we see that in the QCD vacuum there exists a rather small scale of 0.065 fm; such a small scale was already discussed in the studies of QCD vacuum [9, 4].

6. M.I.P. and A.I.V. are grateful to the staff of the Institute for Theoretical Physics of Kanazawa University, where the work was initiated, for their hospitality. This work was supported in part by the Russian Foundation for Basic Research (project nos. 01-02-17456 and 00-15-96786), the INTAS (grant no. 00-00111), the JSPS Grant in Aid for Scientific Research (B) (Grant nos. 10440073 and 11695029), and the CRDF award no. RP1-2103.

REFERENCES

1. T. Suzuki, Nucl. Phys. (Proc. Suppl.) **30**, 176 (1993); M. I. Polikarpov, Nucl. Phys. (Proc. Suppl.) **53**, 134 (1997); M. N. Chernodub and M. I. Polikarpov, in *Confinement, Duality and Non-perturbative Aspects of QCD*, Ed. by Pierre van Baal (Plenum, New York, 1998), p. 387; hep-th/9710205; M. N. Chernodub, F. V. Gubarev, M. I. Polikarpov, and A. I. Veselov, Prog. Theor. Phys. Suppl. **131**, 309 (1998); R. W. Haymaker, Phys. Rep. **315**, 153 (1999).

2. T. L. Ivanenko, A. V. Pochinsky, and M. I. Polikarpov, Phys. Lett. B **252**, 631 (1990); T. L. Ivanenko, A. V. Pochinsky, and M. I. Polikarpov, Phys. Lett. B **302**, 458 (1993).

3. M. Fukushima, A. Tanaka, S. Sasaki, *et al.*, Nucl. Phys. (Proc. Suppl.) **53**, 494 (1997); A. Hart and M. Teper, Phys. Rev. D **58**, 014504 (1998).

4. V. G. Bornyakov, M. N. Chernodub, F. V. Gubarev, *et al.*, Preprint MPI-PHT-2001-06 (March 2001); hep-lat/0103032.
5. H. Suganuma, H. Ichie, A. Tanaka, and K. Amemiya, Prog. Theor. Phys. Suppl. **131**, 559 (1998); H. Ichie and H. Suganuma, Nucl. Phys. B **574**, 70 (2000).
6. M. N. Chernodub, M. I. Polikarpov, and A. I. Veselov, Phys. Lett. B **399**, 267 (1997); N. Nakamura, V. Bornyakov, S. Ejiri, *et al.*, Nucl. Phys. (Proc. Suppl.) **53**, 512 (1997); M. N. Chernodub, M. I. Polikarpov, and A. I. Veselov, Pis'ma Zh. Éksp. Teor. Fiz. **69**, 166 (1999) [JETP Lett. **69**, 174 (1999)].
7. K. Schilling, G. S. Bali, and C. Schlichter, Prog. Theor. Phys. Suppl. **131**, 645 (1998); Nucl. Phys. (Proc. Suppl.) **63**, 519 (1998); **73**, 638 (1999).
8. M. I. Polikarpov and A. I. Veselov, Nucl. Phys. B **297**, 34 (1988); M. G. Perez, T. G. Kovacs, and P. van Baal, Preprint FTUAM-00-13, INLO-PUB-07-00 (May 2000); hep-ph/0006155.
9. K. G. Chetyrkin, S. Narison, and V. I. Zakharov, Nucl. Phys. B **550**, 353 (1999); F. V. Gubarev, M. I. Polikarpov, and V. I. Zakharov, Mod. Phys. Lett. A **14**, 2039 (1999); E. V. Shuryak, hep-ph/9911244.

JETP Letters, Vol. 74, No. 9, 2001, pp. 456–459. Translated from Pis'ma v Zhurnal Éksperimental'noĭ i Teoreticheskoĭ Fiziki, Vol. 74, No. 9, 2001, pp. 511–514.

Oscillating Gap 2π Pulse in Resonantly Absorbing Lattice

B. I. Mantsyzov* and R. A. Sil'nikov

Department of Physics, Moscow State University, Vorob'evy gory, Moscow, 119899 Russia

**e-mail: mants@genphys.phys.msu.su*

Received August 2, 2001; in final form, September 26, 2001

The interaction of a laser pulse with resonant Bragg lattice is studied theoretically for arbitrary initial conditions on the field, inverse population, and polarization of a medium. It is shown that the oscillating 2π self-induced transparency Bragg pulse can form if the Bragg conditions are exactly met. Various regimes are described for the oscillation dynamics of the gap 2π pulse. © *2001 MAIK "Nauka/Interperiodica".*

PACS numbers: 42.25.Fx; 42.50.Md; 42.65.Tg; 42.70.Qs

Over the past decade, the propagation dynamics of laser pulses in the photonic band gap structures, or photonic crystals [1], has been the subject of active studies, both theoretical [2–6] and experimental [7]. Because of the nonlinear interaction of radiation with such structures, the standard linear dispersion relations change qualitatively. As a result, Bragg solitons (BSs) [2–4], i.e., optical pulses with Bragg frequencies, can propagate in the linearly forbidden photonic gaps of the structures with different types of nonlinearity. Contrary to the solitons in continuous medium, the BSs are characterized by two propagation regimes: a regime with a constant velocity and an oscillating regime [5, 6] for which the pulse amplitude and the velocity magnitude and direction change periodically. A resonant oscillating 2π pulse was obtained earlier in [5] by solving numerically the problem on BS in a weakly distorted Bragg lattice. However, the physical nature of BS oscillations has not been revealed because of the lack of analytic solutions. It is shown in this work that the oscillating 2π pulse can arise when the Bragg conditions are exactly met. For the appropriate two-wave Maxwell–Bloch equations, the initial value problem reduces to a modified sine-Gordon equation (SGE). An analytic expression is obtained for the BS oscillation frequency, and the BS propagation regimes are described for different initial conditions.

Let us consider the coherent interaction of an intense laser radiation with a one-dimensional resonant Bragg lattice, whose structure consists of a set of periodically arranged thin layers containing two-level oscillators [2, 5]. This model closely corresponds to a real structure of periodically arranged quantum wells with resonance excitons in semiconductors [7]. The frequency of incident radiation coincides with the frequency of the two-level transition, and, for the Bragg condition to be met exactly, the structure period should be a multiple of the radiation half-wavelength. Under these conditions, the interaction of radiation with the structure is described by the two-wave Maxwell–Bloch equations [2] for real functions in the dimensionless variables $x = x'/c\tau_c$ and $t = t'/\tau_c$

$$\begin{gathered}\Omega_t^+ + \Omega_x^+ = P, \quad \Omega_t^- - \Omega_x^- = P, \\ P_t = n(\Omega^+ + \Omega^-), \quad n_t = -P(\Omega^+ + \Omega^-),\end{gathered} \tag{1}$$

where $\Omega^\pm = (2\tau_c\mu/\hbar)E^\pm$; $E^\pm$ are the smooth field-amplitude envelopes of the forward and backward Bloch waves; τ_c is the cooperative time; μ is the matrix element of the dipole transition moment; P and n are the polarization and density of inverse population, respectively; c is the speed of light; t' and x' are, respectively, the time and spatial coordinate along the normal to the resonance planes in the structure; and the subscripts x and t imply partial derivatives.

By using the solution $P = -\sin\theta$ to the Bloch equations, where the Bloch angle θ is determined from the condition $\theta_t = \Omega^+ + \Omega^-$, Eq. (1) can be rewritten as

$$\tilde{\Omega}_x + \Omega_t = -2\sin\theta, \quad \Omega_x + \tilde{\Omega}_t = 0, \tag{2}$$

where $\Omega \equiv \Omega^+ + \Omega^-$ and $\tilde{\Omega} \equiv \Omega^+ - \Omega^-$. From the second equation in Eqs. (2) it follows that

$$\tilde{\Omega}(x, t) = -\theta_x(x, t) + f(x). \tag{3}$$

Then the following equations are obtained for the Bloch angle from Eqs. (2):

$$\theta_{xx} - \theta_{tt} = 2\sin\theta + f_x(x). \tag{4}$$

This equation is a modified sine-Gordon equation, with the function $f(x)$ being determined by the initial condition in Eq. (3):

$$f(x) = \tilde{\Omega}(x, 0) + \theta_x(x, 0). \tag{5}$$

0021-3640/01/7409-0456$21.00

Therefore, if the fields and inverse population are absent in a medium at $t = 0$, i.e., if $\tilde{\Omega}(x, 0) = 0$ and $\theta(x, 0) = 0$, or if the stationary BS propagates in the structure and $\tilde{\Omega}(x, t) = -\theta_x(x, t)$ [2], then $f(x) = 0$ and Eq. (4) transforms into the exact SGE describing a nonoscillating gap 2π pulse. In the general case of $f(x) \neq 0$, the BS dynamics differs substantially from that described in [2]. The second term on the right-hand side of Eq. (4) corresponds to the interaction between a kink-solution of the exact SGE and a localized perturbation and gives rise to the oscillating regime of the 2π pulse.

The results of numerical integration of the original set of Eqs. (1) are presented in Fig. 1 for the nonzero initial conditions (5) $f(x) = f(0)\,\mathrm{sech}(\sqrt{2}x - x_0)$. For the low initial BS velocities and $f(0) < 0$ (Fig. 1, curve *a*), the oscillations of the BS amplitude and velocity are harmonic, the soliton shape is virtually identical with that of the solution to the exact SGE, and the oscillating BS is localized near the $f(x)$ function. The oscillation frequency depends on the $f(0)$ value. An increase in the initial velocity leads to a change in the form of oscillations (Fig. 1, curve *b*). It is demonstrated below that these oscillations obey the law of motion in the form of an elliptic sine. Finally, if the initial velocities are high, the soliton escapes from the $f(x)$ localization region and propagates as a free BS with a constant velocity and without oscillations (Fig. 1, curve *c*). As the amplitude of the function in initial condition (5) changes sign, i.e., if $f(0) > 0$, then the BS is repelled from the interaction region and also propagates with a constant velocity and without oscillations (Fig. 1, curve *d*).

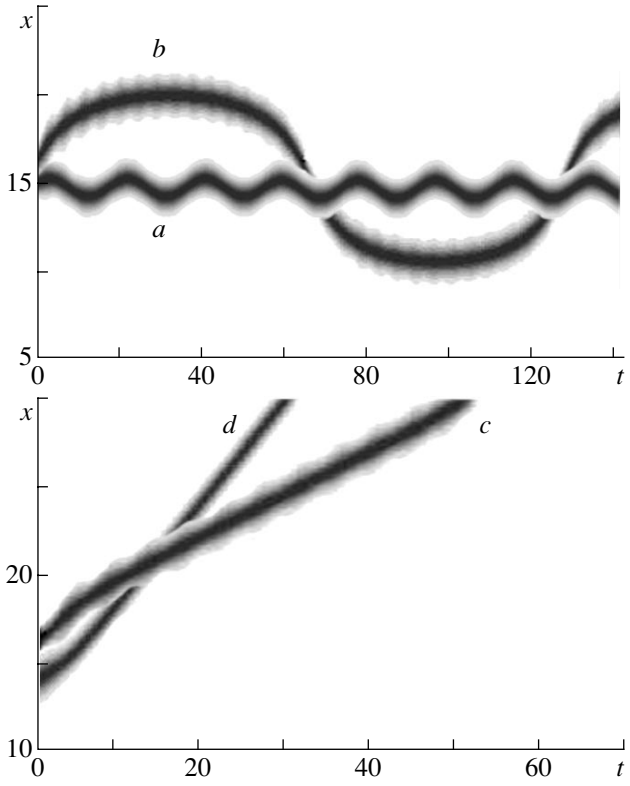

Fig. 1. Equivalue lines for the density $n(x, t)$ of on inverse population in a medium with the Bragg soliton propagating with different initial conditions. The black lines correspond to $n = 1$ and the white background corresponds to $n = -1$. At $t = 0$, the inversion and polarization are given by $n = -\cos(\theta)$ and $P = -\sin(\theta)$, respectively, where $\theta = 4\arctan[\exp(-\sqrt{2}x + x_0)]$ and $x_0/\sqrt{2}$ is the initial coordinate of the soliton center; the fields are $\Omega^{\pm} = \pm\Omega_0^{\pm}\mathrm{sech}(\sqrt{2}x - x_0)$, where $\Omega_0^+ = 1.41$ and $\Omega_0^- = 0.85$ for curve *a* corresponding to the soliton velocity $u = 0.2$; $\Omega_0^+ = 2.12$, $\Omega_0^- = 0.14$, and $u = 0.7$ for curve *b*; and $\Omega_0^+ = 2.21$, $\Omega_0^- = 0.06$, and $u = 0.76$ for curve *c*. In all cases, $f_0 < 0$ and $\sqrt{-f_0} = 0.75$. For curve *d*, $f_0 > 0$ and $\Omega_0^{\pm}$ are the same as for curve *a*.

To analyze this BS dynamics, we use a simple "energetic" method [8], which allows the law of motion to be determined for the soliton of modified SGE (4) in the case where its shape differs only slightly from the shape of the exact solution to the SGE. Let us substitute $\eta = \sqrt{2}x$, $\tau = \sqrt{2}t$, and $f' = f/\sqrt{2}$ and rewrite Eq. (4) in the standard form:

$$\theta_{\eta\eta} - \theta_{\tau\tau} = \sin\theta + f'_{\eta}(\eta). \qquad (6)$$

The Lagrangian density function for Eq. (6) is

$$L = \frac{1}{2}\theta_{\tau}^2 - \frac{1}{2}(\theta_{\eta} - f')^2 - (1 - \cos\theta);$$

the corresponding Hamiltonian density is

$$H = \frac{1}{2}\theta_{\tau}^2 + \frac{1}{2}\theta_{\eta}^2 - f'\theta_{\eta} + \frac{1}{2}f'^2 + (1 - \cos\theta). \qquad (7)$$

Note that the first four terms on the right-hand side of Eq. (7) are equal to the energy density $[(\Omega^+)^2 + (\Omega^-)^2]/2$ of the forward and backward waves in the structure.

Since the system is conservative, the total energy of the localized solutions is the integral of motion, $\frac{d}{d\tau}\int_{-\infty}^{\infty} H d\eta = 0$, so that from Eq. (7) it follows that

$$\frac{d}{d\tau}\int_{-\infty}^{\infty} d\eta\left(\frac{1}{2}\theta_{\tau}^2 + \frac{1}{2}\theta_{\eta}^2 + (1 - \cos\theta)\right) = \frac{d}{d\tau}\int_{-\infty}^{\infty} d\eta f'\theta_{\eta}. \qquad (8)$$

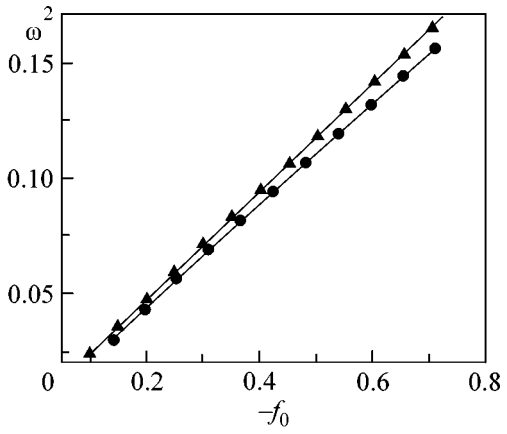

Fig. 2. The square ω^2 of the frequency of harmonic oscillations of the Bragg soliton (ω is in units of τ_c/c) vs. f_0; (▲) are obtained by numerical integration of the set of Eqs. (1) and (●) are calculated using analytic expression (13).

Making use of the fact that the shape of the oscillating soliton given by Eq. (6) differs only slightly from the solution to the exact SGE, one can write the desired solution for a 2π pulse propagating in the positive direction of the η axis as

$$\theta = 4\arctan\left[\exp\left(\frac{-\eta + \xi(\tau)}{\sqrt{1-u^2(\tau)}}\right)\right], \qquad (9)$$

where $u(\tau)$ is the time-dependent soliton velocity and $\xi(\tau) = \int_0^\tau u(\tau')d\tau'$ is the coordinate of the soliton center. The overlap integral on the right-hand side of Eq. (8) is the potential energy of interaction between kink (9) and the perturbation. Substituting Eq. (9) into Eq. (8) and taking into account that u^2 and $u_\tau \ll 1$, one obtains the following equation of motion for the coordinate of pulse center:

$$\xi_{\tau\tau} = -\frac{1}{4}\int_{-\infty}^{\infty} \operatorname{sech}(\eta-\xi)\tanh(\eta-\xi)\, f'(\eta)d\eta. \qquad (10)$$

Let $f'(\eta) = f_0 \operatorname{sech}(\eta)$. The results of numerical integration of the original set of Eqs. (1) with the corresponding initial conditions are shown in Fig. 1. Then it follows from Eq. (10) that

$$\xi_{\tau\tau} = -\frac{f_0}{2}\frac{\sinh\xi - \xi\cosh\xi}{\sinh^2\xi}.$$

This equation can be recast as

$$\xi_{\tau\tau} = -U_\xi, \quad U = \frac{f_0}{2}\frac{\xi}{\sinh\xi}. \qquad (11)$$

Equation (11) describes the quasiparticle motion in the potential U in the field of potential force $-U_\xi$. Since the total "energy" of the particle $u^2/2 + U = \text{const}$, a finite motion is possible only in the attractive potential, i.e., only if $f_0 < 0$, and for a sufficiently low velocity $|u(\xi = 0)| < \sqrt{-f_0}$, i.e., at the bottom of the potential well. This agrees well with the results of numerical calculations (Fig. 1, curve *a*). An increase in the soliton velocity leads to its escape from the potential well (Fig. 1, curve *c*). If the initial conditions (5) are such that $f_0 > 0$, the interaction potential U is positive and the BS is repelled from the perturbation (Fig. 1, curve *d*).

The solution to Eq. (11) gives the law of BS motion $\xi(\tau)$ in the following integral form:

$$\int_0^\xi \frac{d\xi'}{\sqrt{\alpha - f_0\xi'/\sinh\xi'}} = \tau, \qquad (12)$$

where $\alpha = \xi_\tau^2(\xi = 0) + f_0$. By expanding the integrand in Eq. (12) in powers of ξ, one obtains, to second order in ξ, the following expression for the harmonic oscillations of BS with small deviations of the pulse center from equilibrium, $\xi \ll 1$, and $f_0 < 0$:

$$\xi = \xi_0 \sin\omega\tau, \quad \omega^2 = -f_0/6. \qquad (13)$$

To the next order in ξ, the law of motion takes the form of an elliptic sine. The oscillation frequency of a gap 2π pulse, as obtained by the numerical integration of Eqs. (1) and calculated using Eq. (13), is shown in Fig. 2 as a function of f_0. One can see that the analytic formula agrees well with the numerically calculated dynamics of an oscillating 2π pulse.

Note in conclusion that the BS propagation dynamics is more complicated than the dynamics of optical solitons in continuum. This is caused by the interaction of BS with weak fields and medium excitation, which are localized within the Bragg band gap. The oscillating BS is a stable bound state of a high-energy pulse, close to the stationary soliton, and a low-energy perturbation. The latter needs not be necessarily static. The results obtained in this work can easily be extended to the "traveling" initial conditions through the transition to the moving frame of reference. In this case, the mean velocity of the oscillating BS will be nonzero. The oscillating 2π pulse can be observed experimentally, e.g., in the periodic structure of $In_{0.04}Ga_{0.96}As/GaAs$ quantum wells [7, 9], where the density of resonance excitons is 1.7×10^{12} cm^{-3}, the dipole transition moment $\mu = 9 \times 10^{-29}$ C m, the wavelength $\lambda = 830$ nm, and $\tau_c = 0.3$ ps. The corresponding pulse energy per unit area is equal to 1.3 μJ/cm^2 for the oscillating BS at a pulse duration of 0.34 ps.

This work was supported by the Russian Foundation for Basic Research, project no. 01-02-17314.

REFERENCES

1. *Photonic Band Gap Materials*, Ed. by C. M. Soukoulis (Kluwer, Dordrecht, 1996).
2. B. I. Mantsyzov and R. N. Kuz'min, Zh. Éksp. Teor. Fiz. **91**, 65 (1986) [Sov. Phys. JETP **64**, 37 (1986)].
3. W. Chen and D. L. Mills, Phys. Rev. Lett. **58**, 160 (1987).
4. C. Conti, S. Trillo, and G. Assanto, Phys. Rev. Lett. **78**, 2341 (1997).
5. B. I. Mantsyzov, Phys. Rev. A **51**, 4939 (1995).
6. F. De Rossi, C. Conti, and S. Trillo, Phys. Rev. Lett. **81**, 85 (1998).
7. J. P. Prineas, C. Ell, E. S. Lee, *et al.*, Phys. Rev. B **61**, 13863 (2000).
8. M. B. Fogel, S. E. Trullinger, A. R. Bishop, and J. A. Krumhansl, Phys. Rev. B **15**, 1578 (1977).
9. A. Schulzgen, R. Binder, M. E. Donovan, *et al.*, Phys. Rev. Lett. **82**, 2346 (1999).

Translated by V. Sakun

JETP Letters, Vol. 74, No. 9, 2001, pp. 460–463. Translated from Pis'ma v Zhurnal Éksperimental'noĭ i Teoreticheskoĭ Fiziki, Vol. 74, No. 9, 2001, pp. 515–519.

Spectral Superbroadening of Subnanojoule Cr:Forsterite Femtosecond Laser Pulses in a Tapered Fiber

D. A. Akimov[1], A. A. Ivanov[2], M. V. Alfimov[2], S. N. Bagayev[3], T. A. Birks[4], W. J. Wadsworth[4], P. St. J. Russell[4], A. B. Fedotov[1], V. S. Pivtsov[3], A. A. Podshivalov[1], and A. M. Zheltikov[1,*]

[1] *Physics Faculty, International Laser Center, M.V. Lomonosov Moscow State University, 119899 Moscow, Russia*
**e-mail: zheltikov@top.phys.msu.su*

[2] *Center of Photochemistry, Russian Academy of Sciences, ul. Novatorov 7a, 117421 Moscow, Russia*

[3] *Institute of Laser Physics, Siberian Branch, Russian Academy of Sciences, pr. Lavrent'eva 13/3, 630090 Novosibirsk, Russia*

[4] *Department of Physics, University of Bath, BA2 7AY Bath, United Kingdom*

Received September 27, 2001

Abstract—Spectral superbroadening of subnanojoule femtosecond Cr:forsterite laser pulses is demonstrated for the first time in experiments with a tapered fiber. Coupling 40-fs 0.6-nJ pulses of 1.25-μm Cr:forsterite laser radiation into a tapered fiber with a taper waist diameter of about 2 μm and a taper waist length of 90 mm, we observed the spectra spanning more than two octaves at the output of the fiber. These experimental results open new horizons for the creation of compact femtosecond systems based on Cr:forsterite lasers and tapered fibers for optical metrology and biomedical applications. *© 2001 MAIK "Nauka/Interperiodica".*

PACS numbers: 42.65.Wi; 42.81.Qb

Optical fibers of new types—microstructure (holey) [1–6] and tapered [7] fibers—allow the efficiency of spectral broadening of femtosecond pulses [4, 8] and supercontinuum generation [7, 9] to be substantially increased, providing new unique opportunities for optical metrology [10–15], laser biomedicine [16, 17], and spectroscopy. The high degree of light localization in holey and tapered fibers leads to the enhancement of nonlinear-optical interactions, permitting pulses with a spectral width exceeding an octave to be produced at the output of the fiber by coupling unamplified femtosecond pulses with subnanojoule energies into the fiber. This ability of holey and tapered fibers to enhance spectral broadening and supercontinuum generation has recently resulted in a major breakthrough in optical metrology and high-precision optical measurements [10–15] based on the use of frequency combs produced by stabilized mode-locked femtosecond lasers. The idea of applying mode-locked lasers for high-precision frequency measurements has been proposed more than 20 years ago [18, 19]. However, it was not until recently that the practical implementation of this approach became possible due to the rapid progress of femtosecond lasers and the advent of optical fibers of new types, leading to a radical conceptual and technical simplification of high-precision optical frequency measurements.

All the experiments on supercontinuum generation by unamplified femtosecond pulses in microstructure and tapered fibers have been performed so far with Ti:sapphire laser radiation. It is of considerable interest, at the same time, to adapt this technique, allowing the spectral superbroadening of unamplified femtosecond pulses to be achieved, to femtosecond lasers generating radiation with longer wavelengths. In particular, the use of holey and tapered fibers to spectrally broaden and frequency-convert 1.2–1.3-μm femtosecond Cr:forsterite laser pulses is of special interest. Femtosecond Cr:forsterite lasers are as compact and convenient as Ti:sapphire systems, offering, at the same time, several important advantages for establishing a link with methane-stabilized 3.39-μm He–Ne lasers in femtosecond optical metrological systems, as well as for achieving larger penetration depths in optical coherence tomography and biomedical imaging [16, 17]. Investigation of the possibilities to achieve spectral superbroadening of unamplified femtosecond Cr:forsterite laser pulses is the main purpose of this paper.

Our experiments were performed with an all-solid-state self-starting Cr^{4+}:forsterite (Cr^{4+}:Mg_2SiO_4) laser [16, 17], allowing the generation of pulses with a duration of 30–100 fs and the wavelength tunable within the range from 1.21 up to 1.29 μm. A DCDA crystal was used to double the frequency of these pulses [17]. The master oscillator of this laser system (Fig. 1) was based on a Nd:YAG-laser-pumped 19-mm Cr^{4+}:forsterite crystal. The master oscillator also included focusing mirrors with a radius of curvature equal to 100 mm and a 4.5% output coupler. As an option, a semiconductor-saturable-absorber reflector could be used as a rear cavity mirror. Self-starting mode locking in this laser was

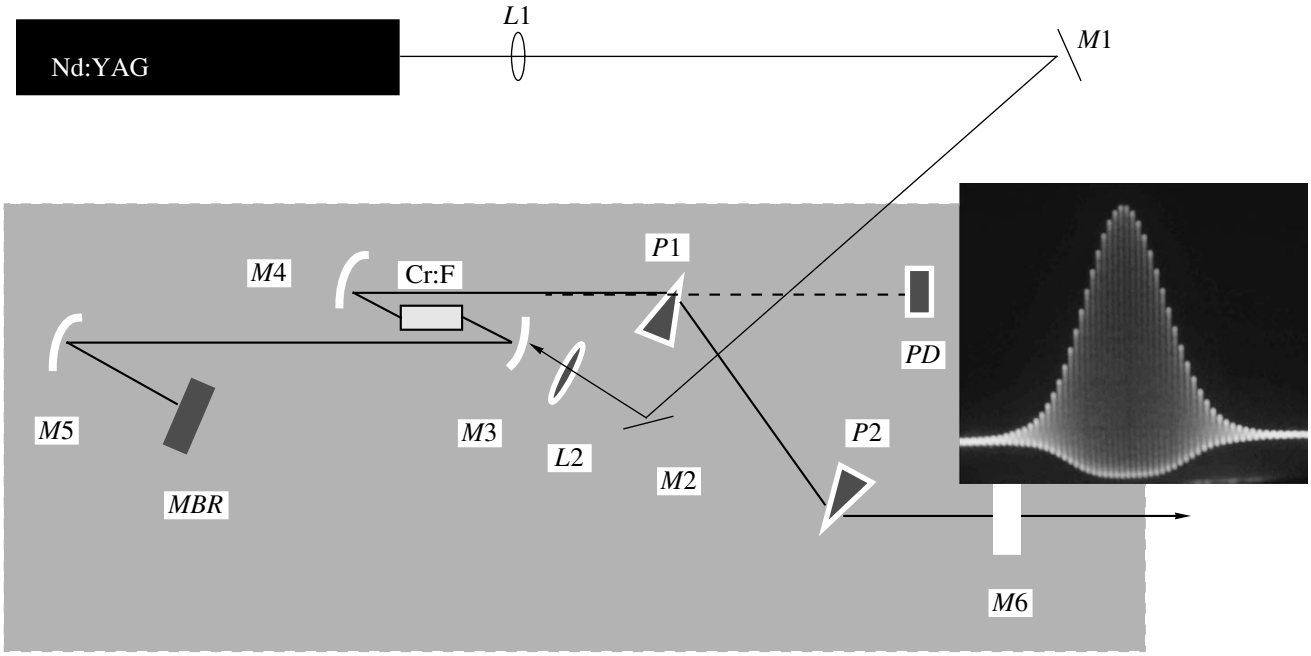

Fig. 1. Diagram of the femtosecond Cr:forsterite laser: Nd:YAG, Spectra Physics Millennia Nd:YAG pump laser; MP1, MP2, pump mirrors; *L*1, *L*2, lenses; *M*3–*M*5, cavity mirrors; *P*1, *P*2, intracavity prisms; Cr:F, Cr^{4+}:Mg_2SiO_4 crystal; *M*6, output coupler; *MBR*, multilayer Bragg reflector; and *PD*, photodetector. The inset shows an autocorrelation trace of a Cr:forsterite laser pulse with a duration of approximately 30 fs.

achieved both with and without semiconductor saturable-absorber mirrors. A typical autocorrelation trace of a 30-fs output pulse of the Cr:forsterite laser is shown in the inset in Fig. 1. With 6–9-W pump; our Cr:forsterite laser generated femtosecond pulses with an average output power of 450 mW.

Unamplified radiation produced by the Cr:forsterite laser was coupled into a tapered fiber, manufactured by tapering Corning SMF-28 standard telecommunications fibers with a core diameter of about 9 μm, a cutoff wavelength of 1250 nm, and a numerical aperture of 0.1. The fiber-tapering procedure was described in detail in [7]. This process involved fiber tapering by means of heating and stretching in a flame, which reduced the fiber cross section. Due to the small fiber diameter in the taper waist region (Fig. 2) and the large refractive index step between silica and air, the light was strongly confined within the fiber, which enhanced the efficiency of nonlinear optical processes. Earlier experiments [20] have demonstrated the enhancement of self-phase modulation in such fibers.

The spectra of 70-fs pulses of different energies coming out of a tapered fiber with a 90-mm waist of a uniform diameter of about 2 m are shown in Fig. 3. The lengths of transition regions of this fiber (Fig. 2) were approximately equal to 35 mm. Tapered fibers with such a waist diameter provide an anomalous dispersion for the fundamental radiation of the Cr:forsterite laser, with a zero group-velocity dispersion being achieved around 700 nm. This situation is favorable for the nonlinear propagation of ultrashort Cr:forsterite laser pulses and for supercontinuum generation in the visible range. We were able to achieve a considerable spectral broadening even with 0.1-nJ light pulses coupled into the fiber. Increasing the energy of laser pulses, we observed the growth in the bandwidth of pulses coming out of the fiber (Fig. 3). To get an order-of-magnitude estimate on the characteristic parameters of the self-phase modulation process, we approximate the dependence of the spectral broadening (on the energy of laser pulses coupled into the fiber with a linear function (see the inset in Fig. 3)). This approximation is based on the elementary theory of self-phase modulation, which gives the following expression for the relative spectral broadening: $\Delta\omega \approx \gamma PL/\tau$, where γ is the nonlinear coefficient, P is the laser pulse power, L is the length of the

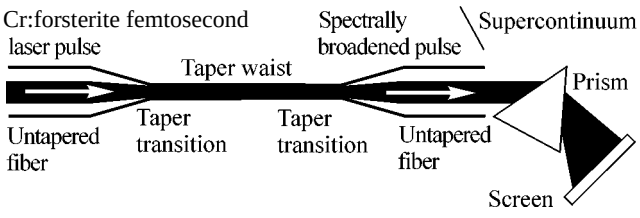

Fig. 2. Diagram of Cr:forsterite pulse propagation through a tapered fiber.

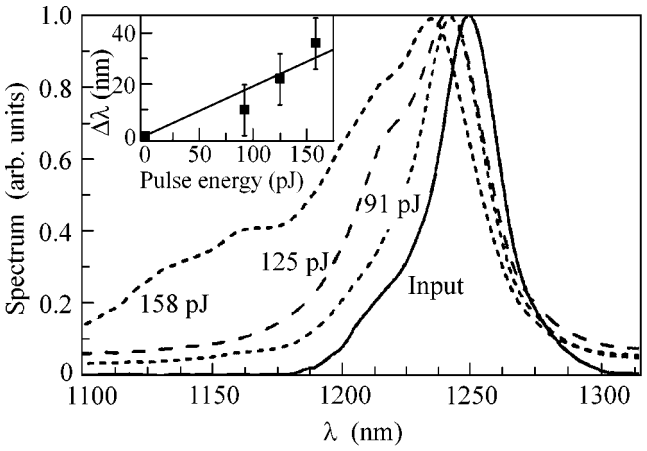

Fig. 3. Spectral broadening Δλ of subnanojoule 70-fs Cr:forsterite laser pulses in a tapered fiber with ~35-mm transitions and a 90-mm waist of a uniform diameter of about 2 μm. Solid line *1* shows the spectrum of the input pulse. Lines *2–4* display the spectra of the pulses at the output of the fiber with (*2*) 0.09, (*3*) 0.13, and (*4*) 0.16 nJ of pulse energy coupled into the fiber. The inset shows the spectral broadening as a function of the pulse energy coupled into the fiber approximated with a linear dependence.

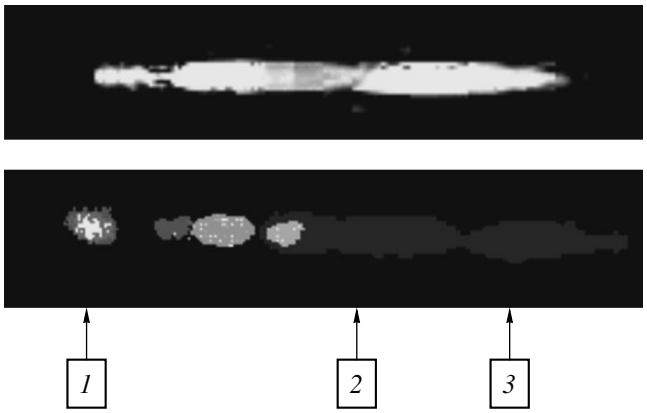

Fig. 4. Digital-camera images of a laser pulse coming out of the tapered fiber dispersed with a prism. A 40-fs 0.6-nJ pulse of 1.25-μm Cr:forsterite laser radiation was coupled into the fiber. The digital camera is located at a distance of 40 cm (the upper image) and 10 cm (the lower image) from the screen. Region *1* corresponds to the visible red, region *2* is the third-harmonic area around 417 nm, and the area of screen luminescence (*3*) corresponds to radiation wavelengths less than 400 nm.

working area of the fiber, and τ is the pulse duration. The nonlinear coefficient estimated in this approximation from our experimental data (Fig. 3) with $n_2 \approx 2.5 \times 10^{-16}$ cm^2/W indicates a very high efficiency of nonlinear optical processes in the tapered fiber.

In contrast to the regime of supercontinuum generation, the initial stage of spectral broadening considered above does not lead to very large spectral widths. However, this stage is very useful for many applications due to the fact that the spectral width of unamplified femtosecond pulses can be easily and reproducibly controlled by changing the energy of input pulses in this case. Femtosecond Cr:forsterite laser pulses with a controllable spectral width seem to offer much promise, in particular, for optical coherence tomography with tunable resolution, as well as for numerous spectroscopic applications.

Starting with a pulse energy of 0.6 nJ, a broad continuum emission was observed in our experiments when 40-fs pulses of Cr:forsterite laser radiation were coupled into a tapered fiber with the above-specified parameters. The Cr:forsterite laser generated 40-fs pulses of an average power of 250 mW at a repetition rate of 120 MHz in these experiments, with approximately 70–75 mW of average power being coupled into the tapered fiber. Figure 4 shows digital-camera images of the output light beam dispersed with a prism (Fig. 2) and visualized on a white screen. The upper image is taken with a camera located at a distance of 40 cm from the screen. The image is, therefore, well focused, but the sensitivity of the camera is not sufficient enough to reproduce the red light (around 700 nm, the area *1* in Fig. 4). The lower image is taken with a camera located at a distance of 10 cm from the screen. The red part of the spectrum is clearly seen in this case, but the image is unfocused.

The spectrum shown in Fig. 4 spans more than two octaves, stretching beyond the spectral area around 417 nm (region *2* in Fig. 4). The latter wavelength is characteristic of the third harmonic of input radiation and is easily identifiable with the third harmonic of our Cr:forsterite laser radiation produced in a nonlinear crystal. Luminescence of the screen in region *3* in Fig. 4 is indicative of the presence of radiation with wavelengths roughly less than 400 nm. No supercontinuum generation was observed when 30–40-fs subnanojoule Cr:forsterite laser pulses were propagated through standard untapered fibers.

Thus, for the first time, we detected supercontinuum generation with subnanojoule femtosecond Cr:forsterite laser pulses propagating in a tapered fiber. Coupling 40-fs 0.6-nJ pulses of 1.25-μm Cr:forsterite laser radiation into a tapered fiber with a taper waist diameter of about 2 μm and a taper waist length of 90 mm, we ended up with the spectra spanning more than two octaves at the output of the fiber. The table puts the results of our experiments in the context of other works on supercontinuum generation using unamplified femtosecond pulses. The possibility of supercontinuum generation by propagating subnanojoule femtosecond Ti:sapphire laser pulses through microstructure fibers was demonstrated by Ranka *et al.* [9]. This finding has opened new avenues in many areas of ultrafast optics and spectroscopy, leading also to revolutionary changes in optical frequency metrology. The search for a simpler design of a fiber capable of generating a supercon-

Spectral superbroadening of unamplified femtosecond laser pulses

	Holey fibers				Tapered fibers			
	τ, fs	*W*, nJ	*L*, cm	Ref.	τ, fs	*W*, nJ	*L*, cm	Ref.
Ti:sapphire laser	100	0.8	75	[9]	200	3.9	9	[8]
Cr:forsterite laser	No superbroadening has been reported so far; efficient spectral broadening was observed in [21]				40	0.6	9	This work

Note: τ is the pulse duration, *W* is the laser pulse energy, and *L* is the length of nonlinear-optical interaction.

tinuum with low-power femtosecond pulses has given Birks *et al.* [7] the idea of using tapered fibers for this purpose. This concept was successfully demonstrated by supercontinuum generation with unamplified Ti:sapphire laser pulses [7]. In the present paper, we reported for the first time the spectral superbroadening of unamplified femtosecond Cr:forsterite laser pulses propagating through a tapered fiber and demonstrated that subnanojoule energies of femtosecond Cr:forsterite laser pulses may be sufficient, with an appropriate choice of pulse durations and fiber dispersion, to generate light with a spectrum spanning more than two octaves. The results of our experiments allow a system including a femtosecond Cr:forsterite laser and a tapered fiber to be proposed as a convenient and compact tool for optical metrology and biomedical applications, as well as an efficient broadband source for various spectroscopic applications.

This work was supported in part by the President of Russian Federation grant no. 00-15-99304; the Russian Foundation for Basic Research project no. 00-02-17567; Volkswagen Foundation project I/76 869; CRDF grants RP2-2266 and RP2-2275; and the "Fundamental Metrology" Federal Program of the Ministry of Industry, Science, and Technology of the Russian Federation.

REFERENCES

1. J. C. Knight, T. A. Birks, P. St. J. Russell, and D. M. Atkin, Opt. Lett. **21**, 1547 (1996).
2. J. C. Knight, J. Broeng, T. A. Birks, and P. St. J. Russell, Science **282**, 1476 (1998).
3. R. F. Cregan, B. J. Mangan, J. C. Knight, *et al.*, Science **285**, 1537 (1999).
4. A. B. Fedotov, A. M. Zheltikov, L. A. Mel'nikov, *et al.*, Pis'ma Zh. Éksp. Teor. Fiz. **71**, 407 (2000) [JETP Lett. **71**, 281 (2000)].
5. T. M. Monro, P. J. Bennett, N. G. R. Broderick, and D. J. Richardson, Opt. Lett. **25**, 206 (2000).
6. A. M. Zheltikov, Usp. Fiz. Nauk **170**, 1203 (2000).
7. T. A. Birks, W. J. Wadsworth, and P. St. J. Russell, Opt. Lett. **25**, 1415 (2000).
8. A. B. Fedotov, A. M. Zheltikov, A. P. Tarasevitch, and D. von der Linde, Appl. Phys. B: Lasers Opt. **B73**, 181 (2001).
9. J. K. Ranka, R. S. Windeler, and A. J. Stentz, Opt. Lett. **25**, 25 (2000).
10. Th. Udem, J. Reichert, R. Holzwarth, and T. W. Häsch, Phys. Rev. Lett. **82**, 3568 (1999).
11. S. A. Diddams, D. J. Jones, Jun Ye, *et al.*, Phys. Rev. Lett. **84**, 5102 (2000).
12. D. J. Jones, S. A. Diddams, J. K. Ranka, *et al.*, Science **288**, 635 (2000).
13. R. Holzwarth, T. Udem, T. W. Hänsch, *et al.*, Phys. Rev. Lett. **85**, 2264 (2000).
14. S. N. Bagayev, S. V. Chepurov, V. M. Klementyev, *et al.*, Appl. Phys. B: Lasers Opt. **B70**, 375 (2000).
15. S. N. Bagayev, A. K. Dmitriyev, S. V. Chepurov, *et al.*, Laser Phys. **11** (12), 1 (2001).
16. A. A. Ivanov, M. V. Alfimov, and A. M. Zheltikov, Laser Phys. **10**, 796 (2000).
17. A. A. Ivanov, M. V. Alfimov, A. B. Fedotov, *et al.*, Laser Phys. **11**, 158 (2001).
18. Ye. V. Baklanov and V. P. Chebotayev, Appl. Phys. **12**, 97 (1977); S. N. Bagayev, V. P. Chebotayev, V. M. Klementyev, and O. I. Pyltsin, in *Proceedings of the 10th International Conference on Laser Spectroscopy, Font-Romeau, France, 1991*.
19. J. N. Eckstein, A. I. Ferguson, and T. W. Hänsch, Phys. Rev. Lett. **40**, 847 (1978).
20. P. Dumais, F. Gonthier, S. Lacroix, *et al.*, Opt. Lett. **18**, 1996 (1993).
21. A. B. Fedotov, V. V. Yakovlev, and A. M. Zheltikov, in *Technical Digest of the 11th International Laser Physics Workshop (LPHYS'2002)* (in press).

Translated by A. Zheltikov

JETP Letters, Vol. 74, No. 9, 2001, pp. 464–466. From Pis'ma v Zhurnal Éksperimental'noĭ i Teoreticheskoĭ Fiziki, Vol. 74, No. 9, 2001, pp. 520–522.

The Possibility of ESCA Microscopy with Laser Femtosecond EUV X-Ray Pulses[1]

V. S. Letokhov

Institute of Spectroscopy, Russian Academy of Sciences, Troitsk, Moscow region, 142190 Russia

Received October 4, 2001

This letter proposes photoelectron spectroscopy (ESCA) for the observation of a 2D molecular structure with nanometer spatial resolution and chemical selectivity using EUV X-ray femtosecond laser pulses. © *2001 MAIK "Nauka/Interperiodica".*

PACS numbers: 33.60.Fy; 42.50.Vk; 82.80.Pv

Femtosecond pulses amplified to ultrahigh intensities [l] enable one to obtain high-order femtosecond harmonics in the EUV and soft X-ray regions [2, 3]. This is of principal importance, for this method makes it possible to transfer coherence from the optical to the X-ray region of the spectrum. In this case, there is no need to make radiation coherent by means of positive feedback, this being very difficult to implement in the X-ray region on a femtosecond time scale. This letter proposes the method for studying the structure of individual biomolecules on the basis of the joint use of optical and EUV X-ray femtosecond laser pulses. Gaining direct information on the molecular structure of individual biomolecules, especially such as DNA and proteins, is a very important problem facing physicists developing new techniques and instruments for other domains of science (one can cite, as an example, X-ray crystallography, electron microscopy, etc.). The requirements on the potential method are exceptionally stringent: (l) atomic specificity, (2) ultrahigh sensitivity, and (3) nm–Å spatial (lateral, longitudinal) resolution. Combining all the above characteristics in one method would make it possible to determine the 3D molecular structure of *individual* biomolecules.

The following methods can be regarded as promising. First, these include femtosecond versions of the well-known classical X-ray diffraction and electron diffraction techniques, because each is capable of being extended to atomic-resolution holography. These techniques, however, require that the specimens be either crystals or ensembles of oriented molecules. Moreover, for these techniques to be implemented, it is necessary that many X-ray photons or electrons be coherent in individual shots. The latter requires intense X-ray radiation, which can cause damage to the structure of specimens on a femtosecond time scale [4].

An alternative is to extend the well-known ESCA technique [5]. This technique is incoherent and can be used with individual biomolecules, while the information can be accumulated in the course of many irradiation pulses of not-too-high intensity. Besides, the photoionization cross section of atoms exposed to X-rays is much larger than the scattering cross section.

To obtain a 2D image of a surface under study, one has to discard the traditional electron spectroscopy techniques; i.e., one should use the time-of-flight method for selecting photoelectrons. It is precisely for this purpose that the possibilities of jointly using femtosecond optical and X-ray pulses prove to be very suitable.

Figure 1 is a simplified illustration of the idea of ESCA microscopy where atoms of the desired element in an individual molecule are ionized by focused X-ray pulses having an energy of $h\nu_X$. The focal spot diameter d_{foc} is much greater than the wavelength λ_X of the X-ray radiation and the size a of an individual molecule containing N ionizable atoms. The ionization probability of one such atom $Y_{ph.ion}$, which depends on the X-ray pulse fluence $\Phi_X/h\nu_X$ and the photoionization cross section $\sigma_{ph.ion}$ ($Y_{ph.ion} \simeq \sigma_{ph.ion}\Phi_X$), is taken to be low ($<1/N$). In this case, one X-ray pulse gives birth to no more than one photoelectron ($NY_{ph.ion} \lesssim 1$). This excludes the Coulomb repulsion of the photoelectrons produced with a low kinetic energy $E_{ph.el}$. An electron-optical system directs these photoelectrons on the surface of a position-sensitive time-resolved (time-of-flight) electron-detection system.

By appropriately selecting the X-ray quantum energy $h\nu_X$, one can ensure the necessary atomic specificity of photoionization [5].

Ultrahigh sensitivity can be attained without damaging the biomolecule by the focused X-ray pulses, if their energy fluence is taken to be adequately low. Consider, as an example, the case where the photoionization cross section $\sigma_{ph.ion} \simeq 10^{-20}$ cm^2 ($h\nu_X \simeq 1$ keV). If an X-ray pulse with energy $E \simeq 1$ nJ in the spectral range $\Delta E \simeq 1$ eV is focused onto the area of size $a \simeq$

[1] This article was submitted by the author in English.

10 μm [this corresponds to $h\nu_X\Phi_X \simeq 1$ mJ/(cm^2 pulse eV)], the ionization probability of a single desired atom may be as high as 10^{-7} photoelectron/(atom pulse), so that for a molecule with $N \approx 10^5$ atoms it will be $Y_{\text{ph.ion}} \approx 10^{-2}$ photoelectron/(molecule pulse). The energy of the X-ray pulse can probably be increased by a factor of 10^2 [up to 0.1 J/(cm^2 pulse eV)] in order to produce approximately one photoelectron per pulse in the biomolecule.

Photoelectrons are produced at the X-ray penetration depth, which is much larger than the monolayer thickness. To achieve surface (monolayer) selectivity, it is necessary to eliminate the background noise caused by the photoelectrons formed in the bulk of a specimen. To this end, use can be made of the effect of photoelectron escape depth minimum $E_{\text{ph.el}}^{\min} \simeq 30$ eV [6]. Selective detection of surface photoelectrons can be accomplished by at least two methods. First, one can use X-ray radiation with energy $h\nu_X = I + E_{\text{ph.el}}^{\min}$. This may be a monochromatized radiation of higher harmonics of laser pulses within a broad X-ray spectral range. Second, one can perform selective detection of photoelectrons with kinetic energy $E_{\text{ph.el}} \approx 30$ eV. In our case of constructing a photoelectron image, this can be attained by means of time-of-flight (TOF) photoelectron detection. The selection of photoelectrons having the required energy $E_{\text{ph.el}} \approx 30$ eV (velocity $v_e \approx 3 \times 10^8$ cm/s) in the energy range ΔE_{resol} on the photoelectron flight path of length $L_{\text{el.fl}} \approx 1$ mm requires that the TOF system used have a very high time resolution at a level of $\tau_{\text{resol}} \approx 10^{-12}$ s. In principle, this is quite possible if a portion of energy of the initial high-intensity optical femtosecond pulses generating the X-ray pulses is used. This possibility is based, in particular, on the electron reflection from the strong light field of femtosecond optical pulses [7].

Figure 2 schematically illustrates the idea of electron reflection from the strong field of an evanescent light wave, as suggested in [7]. The intense evanescent wave formed upon the total internal reflection of a femtosecond light pulse penetrates into a vacuum at a depth on the order of wavelength λ. A change in the electron velocity can be described in terms of the effective index of refraction $n_{el} < 1$[7]:

$$n_{el} = \left[1 - \left(\frac{\mu^2}{\beta^2}\right)\sqrt{1-\beta^2}\right]^{1/2}, \qquad (1)$$

where $\beta = v_e/c$, $\mu^2 = \frac{r_e}{mc}\lambda^2 I$, v_e is the electron velocity, r_e is the classical electron radius, I is intensity, and λ is wavelength. At the intensity in the range 10^{13}–10^{14} W/cm^2, n_{el} drops noticeably for $E_{el} \simeq 10$–100 eV.

Part of the intense femtosecond pulse generating higher harmonics in the X-ray region is also capable of

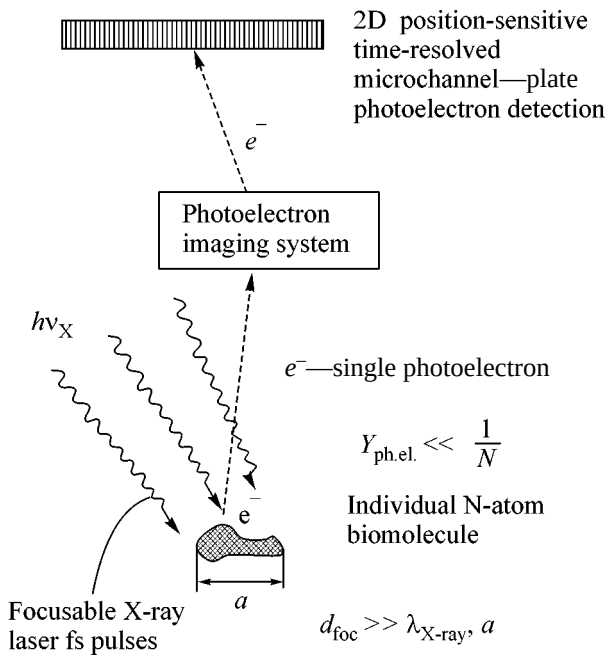

Fig. 1. The simplified general idea of femtosecond ESCA 2D microscopy.

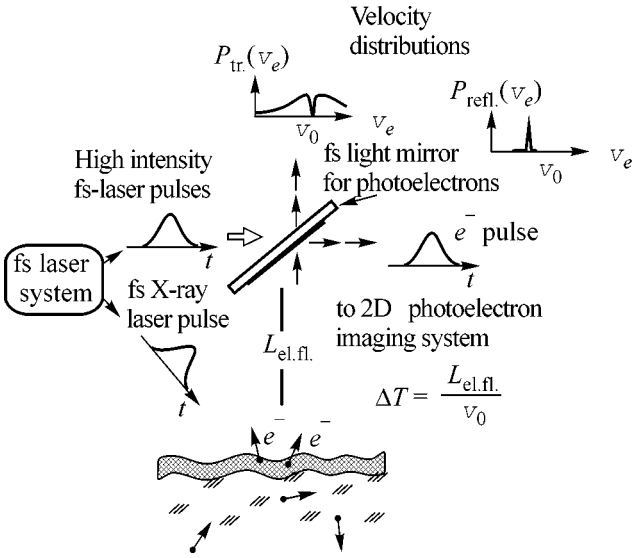

Fig. 2. Idea of time-of-flight photoelectron photoreflection from high-intense femtosecond evanescent light wave.

effectively reflecting electrons with specified velocity v_0, whose time of flight ΔT from the surface is controlled by the time interval between the X-ray and the optical pulses. The reflected photoelectrons with a narrow velocity distribution $P_{\text{refl.}}(v_e)$ should be directed to the imaging system used for 2D visualization purposes.

Naturally, the photoreflection concept presented here has a rather qualitative character because this

effect has not yet been observed experimentally. However, it is of certain interest within the framework of "laser-induced electron optics" [7, 8]. Besides being capable of velocity selection, as discussed above, it provides for the compensation of velocity dispersion for the reflected electrons. Indeed, the slower electrons [at the red edge of the distribution peak $P_{\text{refl.}}(v_{\text{el.}})$] must suffer reflection in a less intense light field of the molecules and cover a shorter distance. The opposite is true for the faster electrons. By using a curved evanescent wave, one can, in principle, attain electron-beam focusing simultaneously with reflection. Of course, all these potentialities of "laser-induced" reflective electron optics should be the subject of future theoretical and experimental studies.

The concept of TOF selection of ejected photoelectrons through femtosecond photoreflection allows one, in principle, to solve the problem of detection of the photoelectrons emerging from a thin surface layer. The problem of attaining high longitudinal resolution necessary for the implementation of 3D microscopy with an atomic-scale resolution still remains to be solved. It is possible that one will have to use an approach based on the consecutive observation of thin surface layers, as demonstrated in [9].

As for the lateral spatial resolution in our experiments with one-photon ionization using laser photoelectron microscopy [10, 11], we achieved a resolution of about 30 nm [12], and the use of a sharp tip and two-photon femtosecond-pulse excitation made it possible to attain a resolution of several 5 nm [13]. Progress in the development of photoelectron microscopy allows one to hope that a resolution on the order of 2 nm will be attained [14]. Therefore, the method proposed in this work is potentially suitable for the table-top sequencing of DNA-like chain molecules with irregularly recurrent molecular blocks spaced at ~1 nm. To solve the entire problem, it is probably necessary to combine several methods in a unified setup.

REFERENCES

1. M. D. Perry and G. Mourou, Science **264**, 917 (1994).
2. A. L.'Hullier and Ph. Balcou, Phys. Rev. Lett. **70**, 774 (1993).
3. T. Guo, C. Spielmann, and C. P. F. Barty, Rev. Sci. Instrum. **72**, 41 (2001).
4. S. Doniach, J. Synchrotron Radiat. **3**, 260 (1996).
5. K. Siegbahn, C. Nordling, A. Fahlman, *et al.*, in *ESCA: Atomic, Molecular and Solid State Structure Studied by Means of Electron Spectroscopy* (Almqvist and Wiksells, Uppsala, 1967), Nova Acta Regiae Soc. Sci. Ups., Ser. 4, Vol. 20; K. Siegbahn, *Nobel Lecture* (1981).
6. *Practical Surface Analysis*, Ed. by D. Briggs and M. R. Seah (Wiley, Chichester, 1990, 2nd ed.).
7. V. I. Balykin, M. V. Subbotin, and V. S. Letokhov, Opt. Commun. **129**, 177 (1996).
8. V. S. Letokhov, Pis'ma Zh. Éksp. Teor. Fiz. **61**, 786 (1995) [JETP Lett. **61**, 805 (1995)].
9. R. Magerle, Phys. Rev. Lett. **85**, 2749 (2000).
10. V. S. Letokhov, Sov. J. Quantum Electron. **5**, 506 (1975).
11. V. S. Letokhov, in *Proceedings of the Conference on Tunable Lasers and Their Applications*, Ed. by A. Mooradian, T. Jaeger, and P. Stokeseth (Springer-Verlag, Berlin, 1976), p. 122.
12. V. N. Konopsky, S. K. Sekatskii, and V. S. Letokhov, Opt. Commun. **132**, 251 (1996).
13. S. K. Sekatskii, S. V. Chekalin, A. I. Ivanov, *et al.*, J. Phys. Chem. A **102**, 4148 (1998).
14. N. Smith, Phys. Today **54**, 29 (2001).

JETP Letters, Vol. 74, No. 9, 2001, pp. 467–470. Translated from Pis'ma v Zhurnal Éksperimental'noĭ i Teoreticheskoĭ Fiziki, Vol. 74, No. 9, 2001, pp. 523–527.

Carbon Systems of Polymerized Nanotubes: Crystal and Electronic Structures

L. A. Chernozatonskiĭ[1, 2], M. Menon[3], T. Yu. Astakhova[1], and G. A. Vinogradov[1]

[1]*Emanuel Institute of Biochemical Physics, Russian Academy of Sciences, ul. Kosygina 4, Moscow, 119991 Russia*

[2]*Lebedev Physical Research Center, Moscow, 119991 Russia*

[3]*University of Kentucky, Lexington, Kentucky 40506-0045, USA*

Received October 5, 2001

Molecular dynamic calculations are carried out for the (*P*, *T*) phase diagram of a covalent compound of cross-linked carbon single-wall nanotubes (SWNT) and for the structures and electronic spectra of the novel crystals of polymerized carbon nanotubes. It is shown that the transformation of covalently bonded nanotubes in a close-packed conducting structure cardinally modifies their electronic properties. The P-SWNT crystal becomes semiconducting and, upon complete transformation of sp^2-hybridized carbon atoms into sp^3-hybridized ones, it becomes an insulator. © *2001 MAIK "Nauka/Interperiodica".*

PACS numbers: 61.46.+w; 61.48.+c; 73.22.-f

The discovery of a large-scale synthesis of single-wall carbon nanotubes [1, 2] and the fabrication of crystals of identical single-wall nanotubes (SWNTs) [3] have generated interest among researches in modeling [4, 5] and synthesizing the SWNT polymeric structures [6] under conditions of high pressures and temperatures, similar to the polymeric structures based on fullerenes C_{60} [7–10]. In recent work [6], a novel superhard material was obtained from the polymerized nanotubes (P-SWNT) under high pressure in a diamond chamber by applying shear strain to a "mat" of bundles of carbon tubes of a nanometer diameter (material from Rice University, Houston, TX, USA [1]). In this work, new structures of covalently bonded carbon SWNTs are modeled together with their electronic properties.

Cross-linking of SWNTs. It is known that the transitions of a C_{60} molecular crystal to layered polymerized phases through [2 + 2] cycloaddition of the C_{60} molecules occur at temperatures $T \approx 700$–1000 K and pressures $P \geq 4$ GPa [8]. It is natural to expect that the phase transitions with the formation of the [2 + 2] rings will occur in the SWNT molecular crystal in the same (*T*, *P*) range (see below structures **1** and **3**). For this reason, we first examined the cross-linking process for nanotubes by the molecular dynamic method using the nonlocal Brenner potential [11], which showed itself good in describing carbon clusters. The forces were calculated analytically as the derivatives of this potential with respect to the radius vector, and the structure temperature was specified by the particle mean velocity. Integration with respect to time was carried out by the Verlet–Birman method. The addition reaction between the (5, 5) and (9, 0) tubes of diameter 0.7 nm intersecting at a right angle was calculated in the temperature range 2100–1100 K for different pressures (1–15 GPa) applied to the intersection region with an area of $\approx 10^{-15}$ cm^2. The process was considered in the regime of constant forces applied to the ends of the nanotube sections of length ≈50 Å comprising 806 carbon atoms (inset in Fig. 1). The evolution time was limited by ~1000 of 0.0003-ps steps. The "phase"-separation curve is shown in Fig. 1, where the temperatures are shown at which the thermalization occurred within the picosecond interval chosen and the tubes were linked together by two to four sp^3 bonds at the intersection site (inset A in Fig. 1). One can see that the reaction temperature decreases dramatically with pressure buildup to 1 GPa and shows quasi-linear behavior above 4 GPa. The approximation to room temperatures, $T \approx 300$ K, gives $P \approx 35$ GPa, which coincides by an order of magnitude with the experimental value of 24 GPa [6]. This curve is qualitatively similar to the (*P*, *T*) diagram for the transition of molecular fullerite C_{60} into polymeric phases [9].

P-SWNT Crystals. Six types of cycloadditions between polyhedral carbon clusters are known: [2 + 2], [2 + 4], [4 + 4] [7–9], [3 + 3] and the formation of a generalized four-membered Osawa ring [10], and the addition of six hexagon atoms to the neighboring hexagon [15]. Among them, the [2 + 2] cycloaddition yields the most energetically stable structures, which form at the initial polymerization step of cluster dimerization. We primarily chose examples with the polymerization of nanotubes in conducting molecular crystals, i.e., the armchair (*n*, *n*) and zigzag (*n*, 0) nanotubes with $n = 3q$ [2] and diameter close to 1 nm, in order to demonstrate the most significant transformations of electronic properties upon the formation of polymeric phases in such crystals. The (6, 6) SWNT crystals were chosen because the electronic structure of the molecular phase

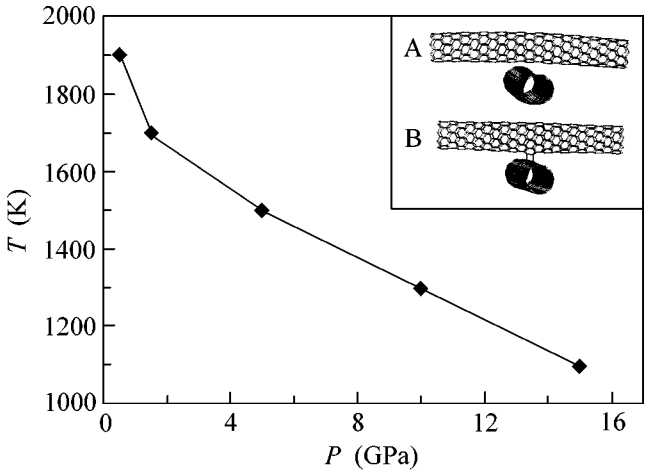

Fig. 1. Phase *T–P* diagram for the polymerization of (5, 5) and (9, 0) nanotubes intersecting at a right angle. The nanotube structures (A) before and (B) after the [2 + 2] cycloaddition are shown schematically in the inset.

of SWNT crystal had been calculated only for the (6, 6) nanotubes, and it was found to be semimetal, like graphite [12]. By the hexagonal symmetry and tube diameter, the structure formed by zigzag (12, 0) nanotubes is most suitable for this crystal. The theoretical study of these P-SWNT crystals was carried out using the molecular mechanic MM+ method [4] (for the preliminary structural calculations) and the generalized tight-binding molecular dynamic GTBMD scheme [13] (for the final calculations of structures and electronic spectra), which were previously used for calculating the equilibrium geometries and electronic spectra of fullerenes and nanotubes and showed a good agreement with the experimental data and calculations by other methods [4, 14]. The GTBMD method allows the interatomic interactions in covalent systems and their full relaxation to be taken into account without any symmetry constraints. This fast and efficient molecular dynamic method for the calculation of polyatomic structures is based on the use of analytic expressions for the forces as derivatives of the off-diagonal part of the Hamiltonian in the tight-binding approximation [13, 14].

(6, 6) P-SWNT. Let us consider structure **A**, which is formed by the polymerization of the (6, 6) tubes, similar to the well-known [2 + 2] cycloaddition reaction in crystals of two- dimensionally polymerized C_{60} [8]. Of 24 atoms in the unit cell of this crystal, 12 (6×2) are in the tetrahedral environment. As is seen in Fig. 2 (inset), each tube is joined by "diamond ladders" to six neighboring tubes. The resulting hexagonal crystal of symmetry C_{6v} with lattice parameters a = 9.918 Å and c = 2.593 Å has two inequivalent atoms, C(1) (0.378, 0.088, 0.0) and C(2) (0.297, 0.158, 0.5). The interatomic bond lengths (in Å) are $d_{11'}$ = 1.526, d_{12} = 1.500, and $d_{22'}$ = 1.358 within the tube and $d_{11''}$ = 1.520

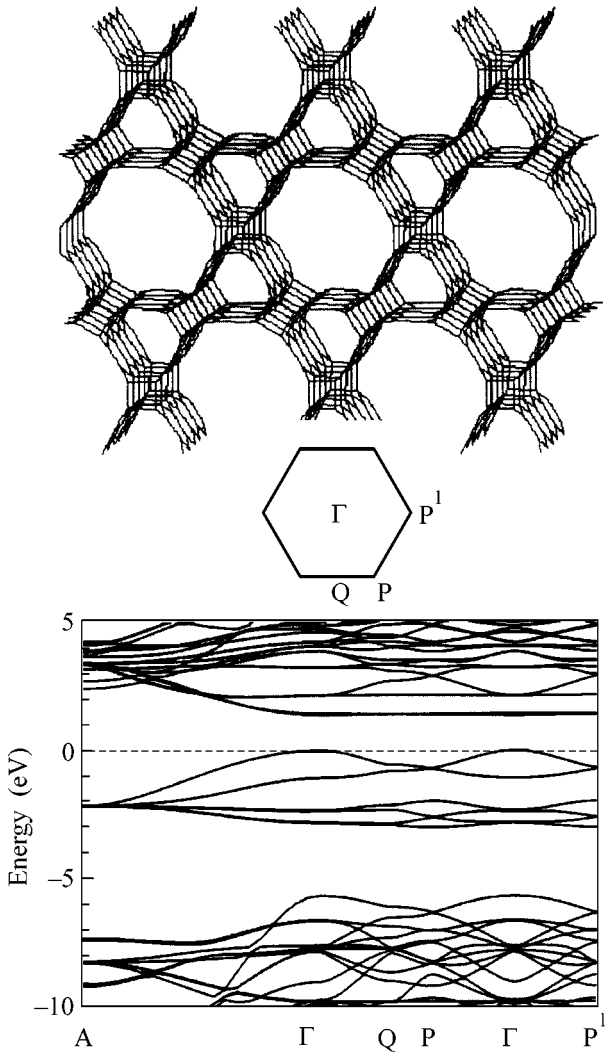

Fig. 2. (top) Perspective drawing of crystal **A** formed by the carbon (6, 6) nanotubes linked together through four-membered [2 + 2] rings, and (bottom) its band structure (the point A corresponds to half of the reciprocal lattice basis vector along the *z* axis coinciding with the nanotube axis). The scheme of hexagonal Brillouin zone in the (k_y, k_z) plane is shown in the middle. The energy gap at the Γ point is equal to 1.3 eV.

between the atoms of neighboring tubes. The density of the P-SWNT crystal under study is 1.22 times higher than the density ρ_0 = 1.79 g/cm^3 of a molecular crystal of the same tubes (ρ_0 was calculated using an estimate of 0.32 nm derived for the intertube distance from the X-ray structural data [1]). The calculated cohesive energy E = –6.85 eV/atom is close to the graphite value of 7.37 eV/atom calculated by the same method [13]. It is seen from the calculated band structure (Fig. 2) that the (6, 6) SWNT crystal has a gap, Δ = 1.3 eV, and should exhibit properties of a direct-gap semiconductor. The valence band is narrow (3.0 eV) and separated from the lower-lying band by a gap of 2.3 eV, giving

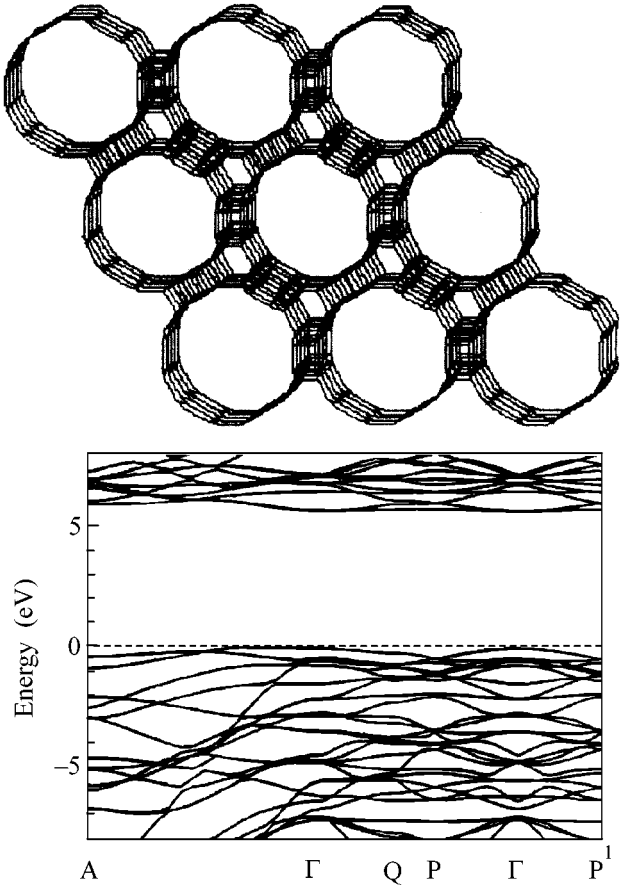

Fig. 3. (top) Perspective drawing and (bottom) band structure of crystal **B** formed by the (6, 6) carbon nanotubes with hexagon–hexagon links. The energy gap at the Γ point is equal to 5.8 eV.

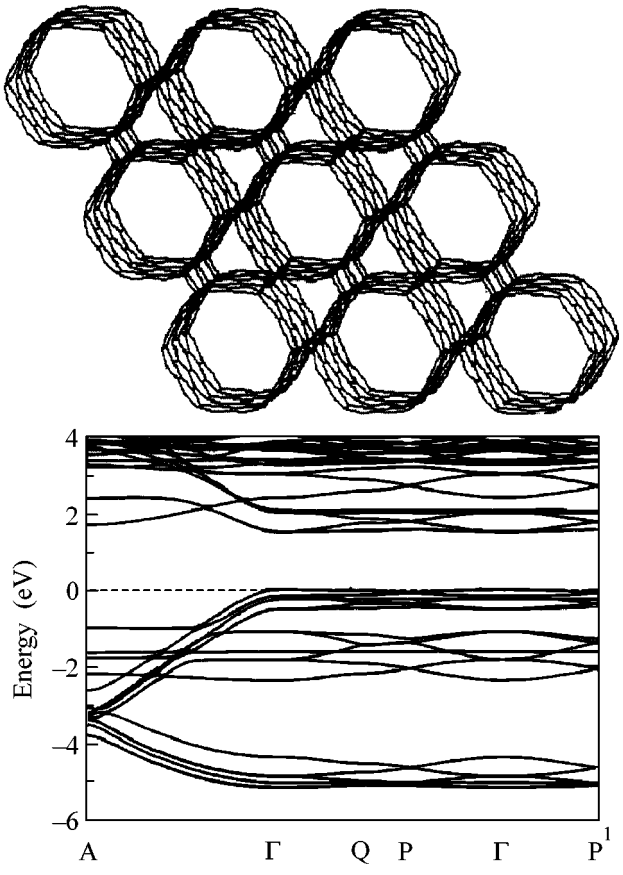

Fig. 4. (top) Perspective drawing of crystal **C** formed by the carbon (12, 0) nanotubes joined together by [2 + 2] rings and (bottom) its band structure. The energy gap at the Γ point is equal to 1.6 eV.

evidence for the insulating effect of the diamond-like interlayers in the carbon superlattice. Thus, the polymerization of (6, 6) nanotubes with sp^3 hybridization of one-half of their atoms results in the transition of the carbon SWNT material from metallic to semiconducting state.

We next consider structure **B**, which is formed by the polymerization of (6, 6) tubes through the hexagon–hexagon linkage [15], i.e., through the formation of six rows of hexagonal prisms formed by the sp^3 atoms along the nanotube axis (Fig. 3). The parameters of a hexagonal unit cell of this P-SWNT crystal are a = 9.883 Å and c = 2.634 Å [inequivalent atoms C(1) 0.377, 0.089, 0 and C(2) 0.330, 0.182, 0.5]. Within the tube, the interatomic bond lengths (in Å) are $d_{11'}$ = 1.522, d_{12} = 1.539, and $d_{22'}$ = 1.476, and the bond lengths between the tubes are $d_{11''}$ = 1.557 and $d_{22''}$ = 1.561. The crystal band structure (Fig. 3) has a gap Δ = 5.8 eV, which is close to the diamond energy gap. The calculated cohesive energy E = –6.11 eV/atom indicates that this compound is less stable than structure **A**, in the same way as the diamond structure relates to the graphite structure. However, a value of 2.16 g/cm^3 found for the density of structure **B** is only 1.21 times larger than the corresponding value in the molecular crystal and, hence, is slightly smaller than for **A**. This fact can be explained by the properties of the structure framework of **A**, where the graphite strip of a nanotube is bent and its curvature changes upon the [2 + 2] cycloaddition [4]. For this reason, structure **A** may be better defined as a hexagonal "pseudographite" structure formed by polymerized (3, 3) nanotubes (its framework is schematically shown in the inset in Fig. 2). Therefore, structure **B** proves to be the lightest among the diamond-like structures whose density is typically 3 g/cm^3 [9].

(12, 0) P-SWNT. Let us now consider structure **C**, which is formed by the polymerization through the [2 + 2] cycloaddition between semimetallic zigzag (12, 0) tubes in the close-packed molecular SWNT structure with density ρ_0 = 1.67 g/cm^3. Of 48 atoms in the unit cell of this crystal, 12 atoms are sp^3-hybridized (Fig. 4). The value of E = –7.19 eV/atom found for it virtually coincides with the graphite cohesive energy. The result-

ing hexagonal crystal of symmetry D_{6h} has lattice parameters $a = 11.53$ Å and $c = 4.30$ Å and a density of 1.94 g/cm^3, which is higher than the density of the molecular crystal by a factor of 1.16. Three equivalent atoms C(1) (0.434, 0, 0.177), C(2) (0.331, 0.121, 0.349), and C(3) (0.226, 0.226, 0.169) are linked together by six bonds: $d_{11'} = 1.524$, $d_{12} = 1.487$, $d_{22'} = 1.401$, $d_{23} = 1.402$, and $d_{33'} = 1.450$ (Å) within the tube and $d_{11''} = 1.522$ Å between the tubes. Due to the polygonization of the cylindrical nanotube surface as a result of breaking it down into strips by the sp^3 atomic chains, electrons cannot freely transfer through the "insulating interlayers" between the strips, giving rise to the gap $\Delta = 1.6$ eV in the electronic spectrum of structure **C** (Fig. 4). Note that a similar effect occurs upon the polygonization of SWNT under a pressure of 3 GPa [16]; for instance, the $(12, 0)^6$ nanotube with a hexagonal cross section has a band gap of 0.5 eV [17].

It should be noted that, due to the intertube covalent sp^3 bonding, the hardness of P-SWNT crystals considered above should be high and comparable with the diamond hardness, as in the structures formed from polymerized 3D C_{60} fullerenes [9, 10]. This fact is confirmed by the synthesis, from the polymerized SWNT, of a material whose hardness (62–85 GPa) is comparable to that of cubic boron nitride [6]. The authors of [6] were of the opinion that they obtained an estimate for the bulk modulus of this material on the basis of an analysis of the behavior of its Raman shift. The corresponding value of 460–540 GPa was higher than the single-crystal diamond value 420 GPa. It is well known that high-hardness materials are characterized by a high bulk modulus **B**. Because of this, we will estimate its value for a polycrystalline P-SWNT structure assuming that it is quasi-isotropic, i.e., that $B = \rho(v_l^2 - 4/3\, v_t^2)$. For structure **C** with the nanotube channels, whose sizes coincide with those of C_{60} fullerenes and the "diamond" bridges between them (the ratio $sp^2/sp^3 = 3$), one can assume that the longitudinal velocity $v_l \approx 21$ cm/s is close to the value of v_l for a graphite sheet (the main contribution comes from the rigid sp^2 bonds) and the transverse velocity $v_t \approx 12$ cm/s is close to the value of v_t in diamond (the main contribution comes from the sp^3 bonds), similar to [10]. The estimate gives for the bulk modulus $B \approx 420$ GPa, which is close to the results obtained in [6]. The detailed calculations of phonon spectra of the structures considered will be published elsewhere.

In summary, the polymerization of single-wall carbon tubes with a nanometer diameter has been modeled in this work, and the geometrical arrangement of atoms in the polymeric SWNT structures is calculated. In particular, a novel tetrahedral (diamond-like) carbon structure **B** with nanotube pores has been considered. It is shown that the electronic spectrum of a crystal formed by carbon nanotubes undergoes substantial modification upon the transition from the molecular phase to the polymerized phase, namely, the metallic state should change to a semiconducting state.

We are grateful to the participants of the physical seminar guided by V.L. Ginzburg and, especially, to Yu.E. Lozovik and I.V. Stankevich and to M. Popov for providing the preprint [6]. This work was supported by the Russian Foundation for Basic Research (project no. 99-02-17578), the Russian program "Fullerenes and Atomic Clusters" (project no. 2-3-99), the NSF (grant no. OSR 99-07463, MRSEC Program under A award no. DMR-9809686), and the INTAS, grant no. 00-237.

REFERENCES

1. A. G. Rintzler, J. Liu, H. Dai, *et al.*, Appl. Phys. A: Mater. Sci. Process. **A67**, 29 (1998).
2. R. Saito, G. Dresselhaus, and M. S. Dresselhaus, *Physical Properties of Carbon Nanotubes* (Imperial College Press, 1998).
3. R. R. Schlitter, J. W. Seo, J. K. Gimzewski, *et al.*, Science **292**, 1136 (2001).
4. L. A. Chernozatonskii, Chem. Phys. Lett. **297**, 257 (1998).
5. L. A. Chernozatonskii, E. G. Gal'pern, N. R. Serebryanaya, and I. V. Stankevich, *Electronic Properties on Novel Materials—Science and Technology of Molecular Nanostructures*, Ed. by H. Kuzmany, J. Fink, M. Mehring, and S. Roth (American Inst. of Physics, New York, 1999), AIP Conf. Proc. **486**, 284 (1999).
6. M. Popov, M. Kyotani, Y. Koga, and R. J. Nemanich, Phys. Rev. B (2001) (in press).
7. A. M. Rao, P. Zhou, K.-W. Wang, *et al.*, Science **259**, 955 (1993).
8. M. Nunez-Regueiro, L. Marques, J.-L. Hodeau, *et al.*, Phys. Rev. Lett. **74**, 278 (1995).
9. V. D. Blank, S. G. Buga, N. R. Serebryanaya, *et al.*, Appl. Phys. A: Mater. Sci. Process. **A64**, 247 (1997).
10. L. Chernozatonskii, Chem. Phys. Lett. **297**, 257 (1998).
11. D. W. Brenner, Phys. Rev. B **42**, 9458 (1990).
12. J. C. Charlier, X. Gonze, and J. P. Michenaud, Europhys. Lett. **29**, 43 (1995).
13. M. Menon, K. R. Subbaswamy, and M. Sawtarie, Phys. Rev. B **48**, 8398 (1993).
14. M. Menon and D. Srivastava, Phys. Rev. Lett. **79**, 4453 (1997).
15. M. O'Keeffe, Nature **352**, 674 (1991).
16. J. Tang, L.-C. Qin, T. Sasaki, *et al.*, Phys. Rev. Lett. **85**, 1887 (2000).
17. J. C. Charlier, Ph. Lambin, and T. W. Ebessen, Phys. Rev. B **54**, R8377 (1996).

Translated by V. Sakun

JETP Letters, Vol. 74, No. 9, 2001, pp. 471–473. Translated from Pis'ma v Zhurnal Éksperimental'noĭ i Teoreticheskoĭ Fiziki, Vol. 74, No. 9, 2001, pp. 528–531.

Reservoir as a Source of Probability in Quantum Mechanics

G. B. Lesovik

Landau Institute for Theoretical Physics, Russian Academy of Sciences, ul. Kosygina 2, Moscow, 117334 Russia

Received August 27, 2001; in final form, October 11, 2001

The concept of the theory of measurement and choice of quantum alternative is considered, according to which the outcome of a particular measurement is determined by the reservoir (detector) state. The way of deducing standard (probabilistic) quantum-mechanical interpretation rules is discussed, with special emphasis on the theoretical demonstration of the wave-function reduction phenomenon. The method of resolving the "Schrodinger cat" paradox is suggested. The interrelation between the mechanisms of formation of shot and flicker noises and the role of reservoir in the formation of quantum-mechanical probability is discussed. © *2001 MAIK "Nauka/Interperiodica".*

PACS numbers: 03.65.Ta; 72.70.+m

The long-standing problem of interpretation of quantum mechanics (QM) has not yet been completely resolved [1]. The proof of wave-function reduction is the key issue in the justification of the standard probabilistic interpretation. However, at present, no theoretical calculation exists[1] that could clearly demonstrate wave-packet reduction (WPR).[2]

In this work, the problem of QM interpretation on the conceptual level and the possible theoretical demonstration of WPR are discussed.

In the standard interpretation, either the WPR problem is considered in isolation from theory or the reduction phenomenon is, in fact, postulated. Let us, for example, cite the textbook of quantum mechanics written by Landau and Lifshitz [2]. In the description of the measurement process (as a unitary evolution of a system), we are led to the point where a wave function appears as a superposition of states corresponding to different readings n of a classical instrument {i.e., as a state of the type of "Schrodinger cat" (SC), which occurs in the superposition of the living and dead states; see [3]}:

$$\psi = \sum_n A_n(x)\Phi_n(X),$$

where x and X are the variables describing, respectively, the particle and the instrument. The authors of the book proceed, "Now, the classical nature of an instrument and the dual role of classical mechanics as a limiting case and, simultaneously, foundation of quantum mechanics come into play … Due to the classical nature of an instrument, its reading at each instant of time … has a certain definite value. One can thus argue that the post-measurement state of a system "instrument + electron" is, in fact, described … only by a single term that corresponds to [a particular] reading of the instrument."

I would also like to add that the instrument, generally, shows a new value in every next measurement, so that one is forced to use the probabilistic description in QM.

Therein lies the central point of the problem. This phenomenon is usually referred to as wave-packet reduction (or wave-function collapse), and the challenge is that nobody knows how to describe this process theoretically. The way of demonstrating technically the WPR will be discussed at the end of this article; nevertheless, the following important conclusions can be drawn from the very assumption that the WPR exists.

If the WPR results from the unitary evolution of the "particle + reservoir" system, then, for a given state of the system, the result may only be unique; i.e., which alternative is precisely realized should become clear from the final wave function. Accordingly, the *outcome of "measurement" should be determined by the initial conditions*.

Inasmuch as it is assumed that the particle wave function is identical in different measurements, one should naturally arrive at the conclusion that it is *the reservoir state which determines the outcome of measurement*.

As to the wave function, it specifies the frequency (probability measure) of a respective outcome. We can say that the degrees of freedom of a reservoir play the role of *nonlocal* hidden Bohm variables in our approach, but the classical reservoir is described not by the "hidden" but by the explicit variables. A one-to-one correspondence between the initial state of the system, "reservoir + particle," and the outcome of measurement is provided by the unitary quantum dynamics of the

[1] To my knowledge.

[2] Some data concerning the decoherence are often regarded as evidence of this phenomenon; one such example with the decay of the off-diagonal part of density matrix is considered in the text.

system. A similar concept has already been proposed by Zurek (see review [4]).

I state, in effect, that the nature of quantum probability is the same as that of classical probability in, e.g., flipping a coin. Whereas the measure of the subspace of initial states for which the coin falls exactly on its edge is vanishingly small in the classical case, in the quantum case this should correspond to the smallness of the measure of initial states evolving into the SC-type state, i.e., into the superposition of macroscopically distinguishable states. Note that quite the reverse is assumed in the many-world interpretation of Everett III [5], according to which the initial states evolving into the superpositions of distinguishable macroscopic states are typical.

Flicker noise. We now present a qualitative argument in favor of the fact that it is the reservoir which is responsible for the outcome of measurement. If the latter was influenced not only by the particle wave function but also by the reservoir state, it would be natural to assume that this influence reduces the accuracy of the "wave function squared" rule and renders it regular only in the idealized situations. Such is indeed the case, and this phenomenon is known as flicker (or $1/f$) noise (hereinafter FN). This noise appears in all nonequilibrium processes, and the preparation and subsequent detection of a large number of particles in one of the states can be regarded as an example of such a process. In the presence of FN, the error rapidly increases with time t, $\delta N \propto t$ (the power of time changes if the spectral density deviates from $1/f$), thereby limiting the highest attainable measurement accuracy. The FN mechanisms in the vast majority of "reasonable" theories amount to the interaction of the detected particles (e.g., electrons in a conductor) with a large number of other degrees of freedom (phonons, photons, impurities, etc.). These degrees of freedom provide for a "flicker" in time, including that on very large time scales. A demonstrative example is provided by the theory of FN in an electronic system interacting only with photons [6]. In this case, there is only one reservoir whose interaction with electrons gives rise to both FN and WPR.[3]

Shot noise. It is customary to assume that, at low temperatures, shot noise appears due to the "quantum-mechanical probability" [7]. Inasmuch as this probability is assumed to be caused by the reservoir, one can state that *the interaction with the reservoir is decisive in the appearance of shot noise.*

We now discuss the problem of the theoretical demonstration of WPR in more detail. The use of a particular model with the aim of tracing the evolution of the total wave function in an explicit form and demonstrating the WPR and the fact that the outcome (e.g., particle location) depends on a particular reservoir state would be the most direct way in this respect. A more standard way consists in the calculation of some quantities averaged over the reservoir state and unambiguously pointing to the WPR. We explore this issue by the example of a particle in a double-well potential (DWP) embedded into a reservoir. This problem was investigated by many authors [8]. In principle, it may serve as a model tool for the description of the measurement process (in the limit of "strong" reservoir) and the demonstration of the transition from quantum to classical behavior.

In the DWP problem, one is usually interested not in the exact coordinate of a particle but in its presence in either of the wells, and the difference $P(t) = P_L(t) - P_R(t)$ in the probabilities (averaged over the reservoir states) of finding the particle in each of the wells is calculated. The fact that, at zero temperature, this difference becomes zero at $t = \infty$ (in a "weak" reservoir, according to [8]) means that $P_L(t) = P_R(t) = 1/2$, and, hence, no localization occurs. At a nonzero temperature, the study of $P(t)$ (averaged over the initial reservoir states) is insufficient for our purpose. For instance, it can turn to zero at large times by different ways. One may imagine that, depending on the reservoir state, either $P_L(\infty) = 1$ and $P(\infty) = 1$ or $P_R(\infty) = 1$ and $P(\infty) = -1$ (as we assume for the "strong" reservoir), so that one obtains $P(\infty) = 0$ only after averaging over all possible reservoir states. However, $P_{L(R)}(\infty) = 1/2$ is also not improbable, or there is a certain distribution function for the probabilities, while the final states are of the SC type, i.e., are coherent superpositions of the left and right states. Note also that the decay of the off-diagonal elements of density matrix

$$\rho(x_L, x_R) = \sum_{X,\beta} \rho_{\beta,\beta} \Psi_\beta(x_L, X) \Psi^*_\beta(x_R, X) = 0$$

($\rho_{\beta,\beta}$ are its diagonal matrix elements in a certain basis set β) also does not rule out the delocalized states of the SC type. Indeed, if the wave function has the form

$$\Psi(x, X) = a_L \Psi_L(x, X) + a_R \Psi_R(x, X),$$

with

$$\int dX \Psi_L(x_L, X) \Psi_R(x_R, X) = 0,$$

and

$$\int dX \Psi^*_{L(R)}(x_{L(R)}, X) \Psi_{L(R)}(x_{L(R)}, X) = 1,$$
$$\int dX \Psi^*_{L(R)}(x_{L(R)}, X) \Psi_{R(L)}(x_{L(R)}, X) = 0,$$

then one can verify that $\rho(x_L, x_R) = 0$ for any coefficients $a_{L(R)}$.

[3] More precisely, we assert that the degrees of freedom localizing a particle give rise to flicker noise, whereas the reverse is not necessarily true: the degrees of freedom relevant to FN may not be crucial to the WPR.

The localization (WPR) phenomenon can be demonstrated after proving the equality

$$L = \langle P_L P_R \rangle$$
$$= \sum_{X, X', \beta} \rho_{\beta,\beta} |\Psi_\beta(x_L, X)|^2 |\Psi_\beta^*(x_R, X')|^2 = 0. \quad (1)$$

The quantity L may serve as an indicator, because it becomes zero only when the SC-type states are excluded (or the measure of such states becomes zero). In the more general case, where the particle coordinate can take many values (as in quantum diffusion [9]), the decay of the quantity

$$L(x_1, x_2)$$
$$= \sum_{X, X', \beta} \rho_{\beta,\beta} |\Psi_\beta(x_1, X)|^2 |\Psi_\beta^*(x_2, X')|^2 = 0, \quad (2)$$

where $x_1 \neq x_2$, may serve as a WPR indicator.

Let us now take the DWP phenomenon as an example to discuss the problem analogous to the SC paradox. Assume that, for a certain reservoir state and fixed particle position at $x = x_L$ or $x = x_R$, the localization (WPR) occurs in the final state. To deduce the "psi squared" rule, one must consider the states for which the particle is initially in the superposition state. Assume that the initial density matrix can be represented as a direct product of the density matrix of the particle in a pure state (a certain superposition of the left and right states) and a certain density matrix of the reservoir. Then it is clear, even without calculations, that, due to linearity, the final state will also be a superposition and will not be localized. In actuality, this is just the SC problem. It is worthy of note that the argument appealing only to the linearity of quantum mechanics is a strong one, so that Schrödinger's mental construction cannot be "bypassed" with ease. To do this, we propose the following variant. I suggest that the state of a system in which a linear superposition is prepared includes, in actuality, a new preparation-reservoir state, which is not a linear superposition of the "typical" reservoir states responsible for the preparation of a particle either on the left or on the right. In other words, *to every initial superposition (spin polarization angle, etc.) there is a unique state of the macroscopic preparation reservoir*, whose effect cannot be ignored. This can be understood from the mere fact that the experimental check of a change in the probabilities of a particle being detected is meaningful only if the possibility exists of comparing with different readings of the instruments controlling the process of superposition preparation; i.e., the states of preparation reservoirs (associated with the instruments) *must be* macroscopically distinguishable. This simple, although very important fact must be taken into account when describing the measurement technique. As applied to the DWP problem, one should explicitly consider the way of preparing a superposition of the left and right states (or, at least, introduce different "replicas" of the Hamiltonian or of the space of states). Of course, it seems somewhat strange that the state of preparation reservoir must be taken into account for the description of measurement, which, possibly, is made far from the preparation site. This question concerning the quantum-mechanical nonlocality will be discussed elsewhere.

It follows from the above arguments that, when preparing the SC, it would be well to start with a linear superposition of macroscopically distinguishable states of the preparation reservoir. However, this is impossible. For the same reasons, one cannot use the results (I am aware of) obtained for the DWP in [8], where a particle was located in one of the wells for an infinitely long time (and, hence, "polarized" the reservoir), to draw any conclusions about the behavior of a particle which was initially in the practically attainable delocalized state.

Note in conclusion that the detailed discussion of the nonstandard interpretations (hidden parameters or many-world interpretation [5]) and philosophical aspects associated with the interpretation of QM were avoided in this letter owing to space restrictions. Some of these issues are discussed in [3, 10].

I am grateful to Vik. Dotsenko, A. Ioselevich, M. Feĭgel'man, and O. Generozova for helpful discussions, which helped me more clearly formulate the concept of the theory of measurement. This work was supported by the Russian Foundation for Basic Research (project no. 00-02-16617), the Ministry of Science (project "Physical Foundations of Quantum Calculations"), the Scientific Foundation of the Netherlands (grant for the collaboration with Russia), and the Swiss Scientific Foundation.

REFERENCES

1. V. L. Ginzburg, Usp. Fiz. Nauk **169**, 419 (1999).
2. L. D. Landau and E. M. Lifshitz, *Course of Theoretical Physics*, Vol. 3: *Quantum Mechanics: Non-Relativistic Theory* (Nauka, Moscow, 1974; Pergamon, New York, 1977), Chap. 1, § 7.
3. R. Penrose, *Shadows of Mind* (Oxford Univ. Press, Oxford, 1994).
4. W. H. Zurek, quant-ph/0105127; submitted to Rev. Mod. Phys. (2001).
5. H. Everett III, Rev. Mod. Phys. **29**, 454 (1957).
6. F. von Oppen and A. Stern, Phys. Rev. Lett. **79**, 1114 (1997).
7. G. B. Lesovik, Pis'ma Zh. Éksp. Teor. Fiz. **70**, 209 (1999) [JETP Lett. **70**, 208 (1999)].
8. A. J. Legget *et al.*, Rev. Mod. Phys. **59**, 1 (1987).
9. W. G. Unruh and W. H. Zurek, Phys. Rev. D **40**, 1071 (1989).
10. B. B. Kadomtsev, *Dynamics and Information* (Izd. Red. Usp. Fiz. Nauk, Moscow, 1999); M. B. Menskiĭ, Usp. Fiz. Nauk **170**, 631 (2000); G. B. Lesovik, Usp. Fiz. Nauk **171**, 449 (2001).

Translated by V. Sakun

JETP Letters, Vol. 74, No. 9, 2001, pp. 474–479. Translated from Pis'ma v Zhurnal Éksperimental'noĭ i Teoreticheskoĭ Fiziki, Vol. 74, No. 9, 2001, pp. 532–538.

BY THE FINAL REPORTS OF PROJECTS SUPPORTED
BY THE RUSSIAN FOUNDATION FOR BASIC RESEARCH,
Project no. 98-02-16897

Electron–Phonon Interaction in a Two-Dimensional Electron Gas of Semiconductor Heterostructures at Low Temperatures

G. N. Gol'tsman and K. V. Smirnov*

Moscow State Pedagogical University, Moscow, 119882 Russia

**skv@mailru.com*

Received October 5, 2001

Theoretical and experimental works devoted to studying electron–phonon interaction in the two-dimensional electron gas of semiconductor heterostructures at low temperatures in the case of strong heating in an electric field under quasi-equilibrium conditions and in a quantizing magnetic field perpendicular to the 2D layer are considered. © *2001 MAIK "Nauka/Interperiodica".*

PACS numbers: 73.50.-h

1. Introduction. Investigation of electron–phonon interaction is one of the central problems in studying two-dimensional (2D) electron systems. The data on this interaction are of great importance in the development and use of a large group of semiconductor devices, for example, detectors based on the electron heating effect [1, 2], and also allow one to considerably extend the understanding of relaxation processes in such systems. Numerous investigations demonstrate that the electron–phonon interaction and the energy relaxation rate in low-dimensional semiconductors differ essentially from those in the case of bulk materials. Basically, the modification of electron–phonon interaction is associated with a change in the electron energy spectrum, because the quantization of the electron energy in the direction perpendicular to the heteroboundary plane becomes important. The phonon energy spectrum in structures with a 2D gas does not change to a first approximation, and the phonons themselves remain three-dimensional, because there is no boundary for phonons between the 2D layer and the bulk material in this approximation. However, as a result of the change in the electron energy spectrum, the conservation laws for energy and momentum impose certain restrictions on the spectrum of phonons interacting with electrons; this fact must be taken into account in studying electron–phonon interaction. Investigations of a 2D layer at the boundary of an AlGaAs/GaAs heterojunction are of most interest among experimental works. This material is characterized by the highest possible mobility of electrons at low temperatures as compared to other materials, which allows electron–phonon interaction in the case of the energy relaxation of 2D carriers to be investigated with great accuracy.

2. Electron–phonon interaction in a 2D gas under equilibrium conditions and strong heating. Theoretical investigations into electron–phonon interaction in two-dimensional structures have long been carried out. Either the temperature dependence of the mobility or the dependence of the energy loss power per electron Q_e on the effective temperature of electrons is commonly considered in these works (see, for example, [3–7]). A typical plot of mobility as a function of temperature is shown in Fig. 1 [8]. Both theoretical curves of the contribution to the mobility due to scattering by phonons and experimental data for an AlGaAs/GaAs heterostructure are presented here. It is evident in the figure that the mobility at low temperatures ($T < 10$ K) is not determined by electron–phonon interaction. The decisive factor in restricting the mobility of carriers is electron–impurity scattering. As the temperature increases, scattering by acoustic phonons becomes more and more prominent. In the cleanest structures, the characteristic temperature separating the temperature region of scattering by impurities from the region in which acoustic electron–phonon interaction dominates shifts toward lower temperatures. It is electron–phonon interaction that determines theoretically the highest possible mobility of the 2D electron gas in AlGaAs/GaAs heterostructures. It was shown in [9, 10] that this value comprises $\mu = 3 \times 10^7$ cm^2 B^{-1} s^{-1} at $T =$ 4.2 K for the 2D concentration of electrons $n_S = 4.2 \times 10^{11}$ cm^2. In the region of high temperatures, the mobility of the 2D electron gas rapidly drops as the temperature increases. Scattering by polar optical phonons is

0021-3640/01/7409-0474$21.00 © 2001 MAIK "Nauka/Interperiodica"

the predominant scattering process at high temperatures.

A detailed theoretical analysis of the dependence of the energy loss power per electron on the electron temperature is given by Karpus [11–14]. Considering various temperature regions for the 2D electron gas of an AlGaAs/GaAs heterojunction under conditions where the first subband of size quantization is almost fully filled (that is, $\varepsilon_F \le W$), Karpus obtained the energy loss power per electron as a function of the electron temperature T_e. In the region of low-angle scattering ($k_BT \ll \sqrt{8ms_\lambda^2\varepsilon_F}$), the energy loss power turns out to be proportional to the third degree of the electron temperature $Q_e \sim T_e^3$. The main mechanism of energy relaxation in this region is piezoacoustic (PA) interaction. As the temperature increases, a transition to a linear dependence $Q_e \sim T_e$ occurs. This dependence is determined by the coexistence of two mechanisms of scattering, namely, scattering by the deformation (DA) and PA potentials.

However, other theoretical estimates also exist for the temperature dependence of the energy loss power in the region in which $k_BT \gg \sqrt{8ms_\lambda^2\varepsilon_F}$, $\sqrt{8ms_\lambda^2 W}$, where scattering by the deformation potentials becomes more and more significant. Thus, it was shown in [15, 16] that scattering by the deformation potential becomes dominant in this region (the contribution of the processes of PA interaction decreases), and the dependence of the total energy loss power per electron can be represented in the form $Q_e \sim (T_e^\gamma - T^\gamma)$, where $\gamma = 2$.

The process of scattering by polar optical phonons becomes the predominant process of scattering in AlGaAs/GaAs heterojunctions at high temperatures. For example, this process was studied theoretically in [17–22]. However, only estimates of the temperature region in which relaxation processes with the participation of optical phonons dominate are given in these works. Thus, it was shown in [22] that the dependence of the energy loss power on the electron temperature in the region of temperatures lower than 40 K is determined by the scattering of electrons by the deformation potential. Scattering by polar optical phonons is the mechanism that determines the temperature dependence of Q_e in the temperature region $T > 50$ K.

A great many experimental studies have been devoted to measuring the energy relaxation rate of 2D electron gas in AlGaAs/GaAs heterostructures. However, measurements of energy losses Q_e under strong heating conditions as a function of the electron temperature T_e have long remained a unique way of determining the energy relaxation rate. As an illustration of this

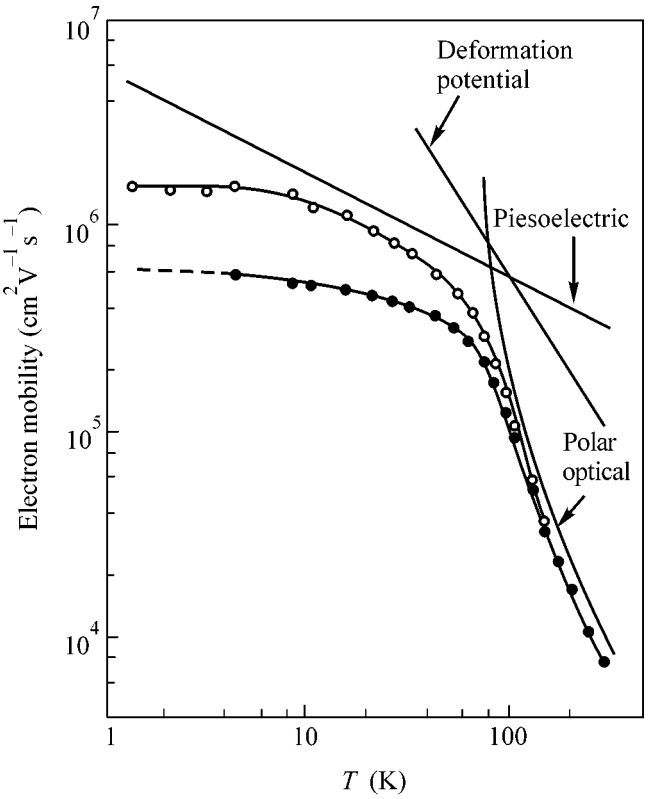

Fig. 1. Temperature dependence of the mobility: theoretical curves and experimental data for two samples of AlGaAs/GaAs heterostructures (from [8]).

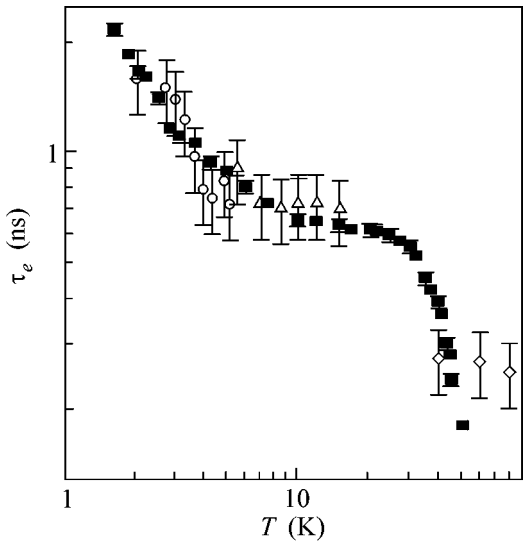

Fig. 2. Temperature dependence of the energy relaxation time. Data from ○ [23], △ [15, 16], ◇ [26], and ■ [9, 10, 28–30].

method, Fig. 2 displays curves $\tau_e(T_e)$ obtained using the known relationships

$$\tau_e(T_e) = \frac{d\varepsilon}{dQ_e(T_e)}, \quad d\varepsilon = \frac{\pi^2 k_B^2 T_e dT_e}{3\varepsilon_F}$$

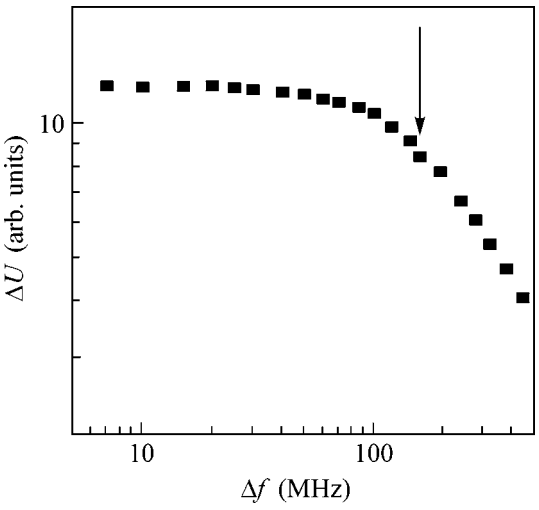

Fig. 3. Typical frequency dependence of the photoconductivity signal from [10]. The arrow indicates the value of f at which $\Delta U = \Delta U_0/\sqrt{2}$.

from the results of measuring $Q_e(T_e)$ in [15, 16, 23]. This figure demonstrates that the error arising in the determination of the energy relaxation time is rather large (~20%). Therefore, based on the data obtained, it is difficult to separate temperature regions in which various mechanisms of electron–phonon interaction dominate. Moreover, the accuracy of the results reported in [15, 16, 23] is limited by the method of determining the electron temperature in heterostructures by the damping of Shubnikov–de Haas oscillations, which is hardly operative at T_e > 15–20 K, that is, under conditions where oscillations are essentially suppressed.

Experiments on determining the characteristic lifetime of an optical phonon τ_{LO} from the luminescence due to the cooling of carriers under pulse interband excitation are close to these works [24–26]. These experiments can give quantitative data on the energy relaxation time only in the region where processes with the participation of optical phonons are pronounced rather well, that is, in the temperature range T_e > 20 K. The interpretation of data in this case is also complicated by the fact that the measured values of τ_{LO} for heterostructures depend significantly on the exciting quantum energy, namely, on its closeness to the band gap energy of the semiconductors that compose the heterojunction. The values of τ_e obtained from [26] are presented in Fig. 2. It is evident that relaxation processes with the participation of optical phonons dominate at temperatures above 40 K. However, in the region of temperatures T_e < 40 K, the Raman lines are only slightly pronounced in the case of the pulse interband excitation of carriers, and experiments on determining the effect of optical phonons on the scattering of hot carriers turn out to be impossible.

A more direct method for determining τ_e based on measuring the time dependence of resistance relaxation in the region of developed Shubnikov–de Haas oscillations upon passing short electric pulses through the sample was used for determining the energy relaxation time of electrons in the 2D gas of AlGaAs/GaAs heterojunctions in [27]. The energy relaxation of 2D carriers was studied in the region in which acoustic scattering dominated (the temperature range T = 4.2–14 K), and the estimate τ_e = 0.5 ns was made. Unfortunately, the effect of a rather strong magnetic field (2–3 T) on relaxation processes was not taken into account in this case. The upper bound on the temperature arose because the method used for determining the energy relaxation time did not work at temperatures at which Shubnikov–de Haas oscillations are essentially suppressed.

Direct measurements of photoresponse relaxation in the millimeter wavelength range allowed the authors [9, 10, 28–30] to determine the inelastic relaxation times of 2D carriers in AlGaAs/GaAs heterostructures under quasi-equilibrium conditions. The essence of the method employed is as follows. The absorption of electromagnetic radiation from two sources of coherent radiation displaced with respect to each other in frequency by Δf leads to electron heating, a change in the mobility, and a change in the dc resistance of the sample. A photoconductivity signal ΔU arises at a frequency of Δf. The photoresponse relaxation time and, hence, the energy relaxation time of carriers are determined by the frequency dependence of ΔU.

A typical amplitude–frequency characteristic of the photoconductivity signal is presented in Fig. 3. The energy relaxation time is determined from the frequency dependence

$$\Delta U(f) = \frac{\Delta U(0)}{\sqrt{1 + (2\pi\Delta f\tau_e)^2}}$$

as $\tau_e = (2\pi\Delta f_0)^{-1}$, where Δf_0 is the frequency at which $\Delta U(\Delta f_0) = \Delta U(0)/\sqrt{2}$. This frequency is shown by the arrow in Fig. 3.

The sensitivity of the apparatus employed allowed measurements to be performed when an increase in the temperature of 2D carriers was only $\Delta T_e \approx 0.1$ K at T = 4.2 K.

The dependence $\tau_e(T)$ obtained experimentally for AlGaAs/GaAs heterostructures with the concentration of 2D carriers $n_s = 4.2 \times 10^{11}$ cm^{-2} and the electron mobility $\mu = 7.5 \times 10^5$ cm^2 V^{-1} s^{-1} at T = 4.2 K is presented in Fig. 2. According to this dependence, the entire temperature range may be divided into four regions. The first region T < 3 K is the region of decreasing energy relaxation time as $\tau_e \sim (T_e)^{-1}$. As was shown by Karpus [11], PA scattering predominates in this region. As follows from the theoretical consideration [11, 31], the second temperature region 3 < T < 10 K corresponds to the coexistence of scattering pro-

cesses determined by the PA potential and DA phonons. As the temperature increases, scattering by the DA potential, which is not revealed at low temperatures, becomes more and more significant, leading to a deceleration of the drop in τ_e as the temperature increases. According to [15, 16], the constancy of the energy relaxation time observed in the temperature range $10 < T < 21$ K (the third region) corresponds to the dominance of DA scattering processes [energy losses of the form $Q_e \sim (T_e^2 - T^2)$]. The value of the relaxation time obtained in [10, 28–30] in this region, $\tau_{DA} = 0.6$ ns, is lower than the value predicted in [16] (~0.9 ns) but is very close to the estimate $\tau_e = 0.5$ ns obtained from the first direct measurements [27].

The authors of [28–30] associate the high-temperature range of the curve $\tau_e(T)$, where a sharp drop in the energy relaxation time is observed ($T > 21$ K), with the effect of optical phonons. Actually, the data obtained on τ_e are close to the theoretical temperature dependence [22]. The characteristic lifetime of an optical phonon determined at $T > 35$ K was found to be $\tau_{LO} \sim 4.5$ ps. This value is 30 times greater than the spontaneous emission time of an optical phonon (equal to 0.15 ps according to an estimate made by the authors of [17]), which is due to processes of phonon reabsorption by electrons.

The dependence of the energy loss rate on the electron temperature can be calculated from the results obtained by the authors of [9, 10, 28–30] (Fig. 4). Experimental data for samples with close concentrations taken from [16, 23, 36] are also plotted in Fig. 4. The values of Q_e obtained under strong dc heating are in a good agreement with the values calculated from the values of τ_e obtained under quasi-equilibrium conditions. This agreement indicates that τ_e is actually a function of only the electron temperature in the entire temperature range.

Note that the contribution of optical phonons to the temperature dependence of the energy relaxation time manifests itself as a sharp drop in τ_e at $T > 25$ K (Fig. 2). In the case of measuring the energy loss power per electron, the effect of optical phonons must be revealed as a deviation from the relationship $Q_e \sim T_e^2$ [11–14], which is characteristic of the region of scattering by the deformation potential. However, it is evident in Fig. 4 that the deviations indicated above are hardly detectable within the experimental error even at $T \sim 40$ K. Thus, the method used by the authors of [9, 10, 28–30] for measuring the energy relaxation time provides more accurate data on the mechanisms of electron–phonon interaction in 2D systems.

3. Electron–phonon interaction in a 2D gas in a magnetic field. Because the density of electron states depends on the magnetic field, the energy relaxation rate must also undergo oscillations similar to Shubnikov–de Haas oscillations. In a real situation, where a system is characterized by disorder, energy relaxation may proceed through both transitions between Landau levels and intralevel transitions. Which of these processes is determining depends on the experimental conditions [32]. It follows from [33] that the energy relaxation rate in the case of intralevel relaxation depends essentially on the density of states and increases for electron–phonon transitions occurring in a region of energies corresponding to a high density of states; that is, the energy relaxation rate is a maximum when the Fermi level coincides with a Landau level, and it is a minimum when ε_F falls in the region of localized states.

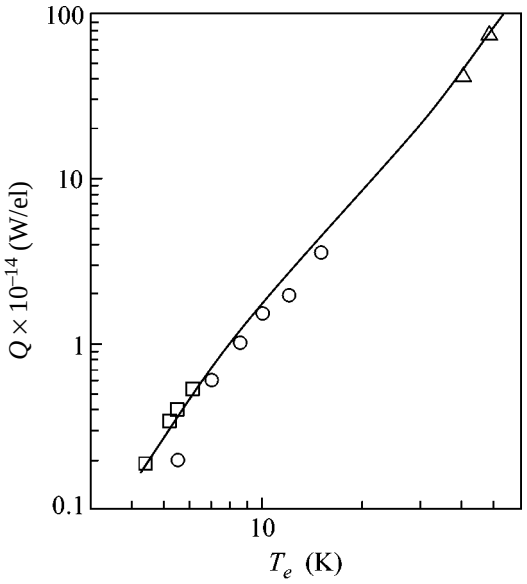

Fig. 4. Dependence of the energy loss power on the electron temperature. The solid curve corresponds to the calculation with τ_e from [9, 10, 28–30]; □ data from [23], ○ data from [16], and △ data from [26].

It is shown in [34–37] that the change in the electron energy spectrum is accompanied by a change in the spectrum of phonons participating in electron–phonon interaction in the magnetic field. In the absence of a magnetic field, electron–phonon interaction involves phonons whose wave vector is restricted in the direction perpendicular to the 2D layer by the transverse layer dimensions $q_\perp < 1/d$, and $q_\parallel < 2k_F$ in the layer plane, in accordance with the conservation laws for energy and momentum. In a magnetic field, $q_\parallel$ is also restricted by the magnetic length $q_\parallel < 1/l_B$, and $q_{\parallel B \neq 0} \ll q_{\parallel B = 0}$ for magnetic fields $B \leq 8$ T at the typical concentration of carriers $n_S \cong 5 \times 10^{11}$ cm^{-2} in GaAs/AlGaAs 2D structures. Thus, whereas the energy relaxation rate in the absence of a magnetic field is determined by the isotropic emission of high-energy phonons, such phonons can be emitted only at small angles to the magnetic field direction in a strong magnetic field. This significantly decreases the energy relaxation rate of electrons.

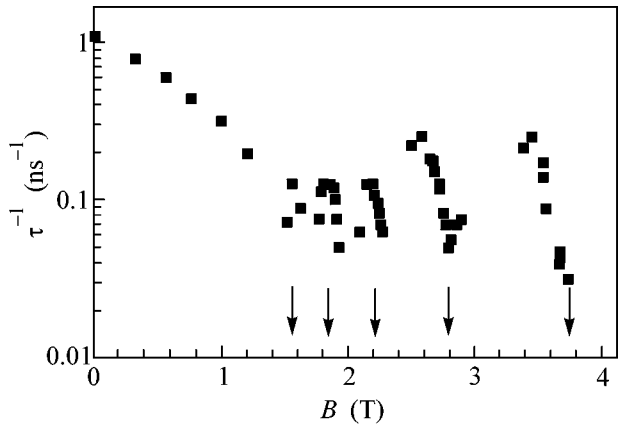

Fig. 5. Dependence of the energy relaxation rate on the magnetic field B (from [39, 40]). Arrows indicate the values of the magnetic field corresponding to a minimum in the oscillation of the Shubnikov-de Haas resistance.

Experimental works devoted to studying the energy relaxation rate of 2D carriers in a magnetic field perpendicular to the 2D plane are mainly concerned with the change in the spectrum of phonons interacting with electrons in the magnetic field and with their angular distribution [33–37]. The energy relaxation time τ_e in the case of interlevel electron transitions was estimated in [38] from the results of measuring the occupation of the Landau levels by magnetotunneling spectroscopy. It was found equal to ~100 ns in the field $B = 4$ T, which is significantly larger than the values of τ_e corresponding to a zero-field case. Direct measurements of the energy relaxation time of 2D electrons τ_e at an AlGaAs/GaAs heteroboundary at 4.2 K under quasi-equilibrium conditions in a magnetic field perpendicular to the 2D plane were performed by the authors of [39, 40], who used the millimeter spectroscopy technique discussed above in detail.

The experimental dependence of the energy relaxation time on the magnetic field B is displayed in Fig. 5. It is evident that, even in low magnetic fields, electron–phonon interaction becomes less efficient as B grows (τ_e^{-1} decreases), and the energy relaxation rate at $B \approx 1.2$ T drops by an order of magnitude compared to its value at $B = 0$. This fact is explained by the change in the spectrum of phonons participating in electron–phonon interaction, as discussed above.

Oscillations are observed in the $\tau_e^{-1}(B)$ dependence in the region of high magnetic fields ($B > 1$ T, filling factor $\nu < 8$). The oscillation depth increases with increasing B. The values of B corresponding to minima in the oscillations of the Shubnikov–de Haas resistance are marked with arrows in the same figure. It is evident that a minimum in τ_e^{-1} is observed at values of B corresponding to a minimum of R at $B > 2.5$ T and to a maximum of R at $B < 2$ T. An analysis of experimental conditions (cyclotron energy, millimeter radiation quantum energy, and kT) indicates that the energy relaxation of carriers in magnetic fields $B > 2.5$ T is accomplished through electronic transitions inside a Landau level. It follows from [33] that the energy relaxation rate in the case of intralevel transitions is minimal when ε_F falls in the region of localized states, that is, in the region of a minimum of R. Interlevel transitions can participate only in the region of low magnetic fields in the transition region $1 < B < 2.5$ T. These interlevel transitions are associated with the fact that several Landau levels become partially filled. In this case, according to [33], the energy relaxation rate is maximal when the Fermi level falls in the region of localized states between Landau levels.

The results of [39, 40] are in accordance with the results of experiments on heating 2D electron gas by an electric field in the presence of a magnetic field [32]. The relationship $Q \sim (T_e^3 - T^3)$ is observed in a wide temperature range. However, starting at a certain value of T_e (which increases with increasing B), the energy relaxation rate significantly increases. The authors associate this observation with the emission of phonons with the cyclotron energy by electrons. They also indicate that transitions of this type are also observed at $\alpha kT_e \approx \hbar\omega_c$, where α assumes values from 2 to 4. This corresponds to magnetic fields $B \sim 1$–1.5 T at a temperature of 4.2 K. It follows from [39, 40] that interlevel electron–phonon transitions start to play the determining role in the same region of magnetic fields.

This work was supported by the Russian Foundation for Basic Research, project no. 01-02-17058.

REFERENCES

1. K. S. Yngvesson, Appl. Phys. Lett. **76**, 777 (2000).
2. Y. Kawano, Y. Hisanaga, H. Takenouchi, and S. Komiyama, J. Appl. Phys. **89**, 4037 (2001).
3. R. F. S. Hearmon, in *Landolt-Börnstein: Numerical Data and Functional Relationships in Science and Technology, New Series* (Springer-Verlag, Berlin, 1979), Group III, Vol. 11, p. 11.
4. P. J. Price, Surf. Sci. **113**, 199 (1982).
5. P. J. Price, Surf. Sci. **143**, 145 (1984).
6. P. J. Price, J. Appl. Phys. **53**, 6863 (1982).
7. C. Weisbuch and B. Vinter, in *Quantum Semiconductor Structures: Fundamentals and Applications* (Academic, Boston, 1991), p. 19.
8. J. J. Harris, J. A. Pals, and R. Woltjer, Rep. Prog. Phys. **52**, 1217 (1989).
9. A. A. Verevkin, N. G. Ptitsina, G. M. Chulcova, *et al.*, Phys. Rev. B **53**, R7592 (1996).
10. A. A. Verevkin, N. G. Ptitsina, G. M. Chulkova, *et al.*, Pis'ma Zh. Éksp. Teor. Fiz. **61**, 579 (1995) [JETP Lett. **61**, 591 (1995)].
11. V. Karpus, Fiz. Tekh. Poluprovodn. (Leningrad) **22**, 439 (1988) [Sov. Phys. Semicond. **22**, 268 (1988)].

12. V. Karpus, Fiz. Tekh. Poluprovodn. (Leningrad) **20**, 12 (1986) [Sov. Phys. Semicond. **20**, 6 (1986)].
13. V. Karpus, Fiz. Tekh. Poluprovodn. (Leningrad) **21**, 1949 (1987) [Sov. Phys. Semicond. **21**, 1180 (1987)].
14. V. Karpus, Semicond. Sci. Technol. **5**, 691 (1990).
15. H. Sakaki, K. Hirakawa, J. Yoshino, *et al.*, Surf. Sci. **142**, 306 (1984).
16. K. Hirakawa and H. Sakaki, Appl. Phys. Lett. **49**, 889 (1986).
17. B. K. Ridley, Rep. Prog. Phys. **54**, 169 (1991).
18. B. K. Ridley, J. Phys. C **15**, 5899 (1982).
19. S. É. Esipov and I. B. Levinson, Zh. Éksp. Teor. Fiz. **90**, 330 (1986) [Sov. Phys. JETP **63**, 191 (1986)].
20. A. Straw, A. J. Vickers, N. Balkan, *et al.*, Superlattices Microstruct. **10**, 203 (1991).
21. Jagdeep Shah, IEEE J. Quantum Electron. **QE-22**, 1728 (1986).
22. N. G. Asmar, A. G. Markelz, E. G. Gwinn, *et al.*, Phys. Rev. B **51**, 18041 (1995).
23. M. G. Blyumina, A. G. Denisov, T. A. Polyanskaya, *et al.*, Pis'ma Zh. Éksp. Teor. Fiz. **44**, 257 (1986) [JETP Lett. **44**, 331 (1986)].
24. J. F. Ryan, R. A. Taylor, A. J. Turberfield, *et al.*, Phys. Rev. Lett. **53**, 1841 (1984).
25. W. Potz and P. Kocevar, Phys. Rev. B **28**, 7040 (1983).
26. R. A. Hopfel and G. Weimann, Appl. Phys. Lett. **46**, 291 (1985).
27. J. Lutz, F. Kuchar, K. Ismail, *et al.*, Semicond. Sci. Technol. **8**, 399 (1993).
28. A. A. Verevkin, N. G. Ptitsina, K. V. Smirnov, *et al.*, Pis'ma Zh. Éksp. Teor. Fiz. **64**, 371 (1996) [JETP Lett. **64**, 404 (1996)].
29. A. A. Verevkin, N. G. Ptitsina, K. V. Smirnov, *et al.*, in *Proceedings of the III All-Russia Conference on the Physics of Semiconductors "Semiconductors'97," 1997*, p. 229.
30. A. A. Verevkin, N. G. Ptitsina, K. V. Smirnov, *et al.*, in *Proceedings of the International Semiconductor Device Research Symposium, Charlottesville, USA, 1997*, p. 55.
31. Y. Ma, R. Fletcher, E. Zaremba, *et al.*, Phys. Rev. B **43**, 9033 (1991).
32. D. R. Leadley, R. J. Nicholas, J. J. Harris, *et al.*, Semicond. Sci. Technol. **4**, 879 (1989).
33. A. J. Kent, R. E. Strickland, K. R. Stpickland, *et al.*, Phys. Rev. B **54**, 2019 (1996).
34. H. A. J. M. Reinen, T. T. J. M. Berendschot, R. J. H. Kappert, *et al.*, Solid State Commun. **65**, 1495 (1988).
35. G. A. Toombs, F. W. Sheard, D. Neilson, *et al.*, Solid State Commun. **64**, 577 (1987).
36. F. Dietzel, W. Dietsche, and K. Ploog, Phys. Rev. B **48**, 4713 (1993).
37. K. Benedict, J. Phys.: Condens. Matter **4**, 4083 (1992).
38. B. R. A. Neves, N. Mori, P. H. Beton, *et al.*, Phys. Rev. B **52**, 4666 (1995).
39. N. G. Ptitsina, A. A. Verevkin, K. V. Smirnov, *et al.*, in *Proceedings of the 24th International Conference on the Physics of Semiconductors, Jerusalem, 1998.*
40. K. V. Smirnov, N. G. Ptitsina, Yu. B. Vakhtomin, *et al.*, Pis'ma Zh. Éksp. Teor. Fiz. **71**, 47 (2000) [JETP Lett. **71**, 31 (2000)].

Translated by A. Bagatur'yants